catalysts

MDPI

Review

The Mechanism of Rubisco Catalyzed Carboxylation Reaction: Chemical Aspects Involving Acid-Base Chemistry and Functioning of the Molecular Machine

Immacolata C. Tommasi

Dipartimento di Chimica, Università di Bari Aldo Moro, 70126 Bari, Italy; immacolata.tommasi@uniba.it

Abstract: In recent years, a great deal of attention has been paid by the scientific community to improving the efficiency of photosynthetic carbon assimilation, plant growth and biomass production in order to achieve a higher crop productivity. Therefore, the primary carboxylase enzyme of the photosynthetic process Rubisco has received considerable attention focused on many aspects of the enzyme function including protein structure, protein engineering and assembly, enzyme activation and kinetics. Based on its fundamental role in carbon assimilation Rubisco is also targeted by the CO_2-fertilization effect, which is the increased rate of photosynthesis due to increasing atmospheric CO_2-concentration. The aim of this review is to provide a framework, as complete as possible, of the mechanism of the RuBP carboxylation/hydration reaction including description of chemical events occurring at the enzyme "activating" and "catalytic" sites (which involve Broensted acid-base reactions) and the functioning of the complex molecular machine. Important research results achieved over the last few years providing substantial advancement in understanding the enzyme functioning will be discussed.

Keywords: enzyme carboxylation reactions; enzyme acid-base catalysis; CO_2-fixation; enzyme reaction mechanism; potential energy profiles

Citation: Tommasi, I.C. The Mechanism of Rubisco Catalyzed Carboxylation Reaction: Chemical Aspects Involving Acid-Base Chemistry and Functioning of the Molecular Machine. *Catalysts* **2021**, *11*, 813. https://doi.org/10.3390/catal11070813

Academic Editor: Arnaud Travert

Received: 6 May 2021
Accepted: 27 June 2021
Published: 1 July 2021

1. Introduction

The increased amount of anthropogenic CO_2 emissions since the beginning of the industrial era (starting around 1750) has significantly affected the natural biogeochemical carbon cycle. An analysis of the components of the anthropogenic "CO_2 budget", as defined in Reports released by the Intergovernmental Panel on Climate Change (IPCC) [1] and the Global Carbon Budget Project [2] (GCB Project, Table S1), show that, since 1750, global CO_2-emissions amounted to about 700 GtC compared to 400 GtC fixed by CO_2-natural sinks (Table S1). Therefore, approximately 285 GtC has accumulated in the atmosphere causing an increase to the actual value of 407 ppm.

However, estimates of carbon fluxes between different compartments of terrestrial ecosystems (Figure S1, Table S2, Supplementary Materials) evidence that, during the last six decades, oceans and land have adapted to such "CO_2 pressure", increasing CO_2 natural sink [2].There is a consensus that terrestrial carbon sink (S_{LAND}, see Section S1) has constantly increased in the Northern Hemisphere largely due to the "CO_2-fertilization effect". This effect accounts for higher rates of photosynthesis and, consequently, for increase of plant Gross Primary Production (GPP) due to rising atmospheric CO_2 concentration [3,4] strengthened by concomitant increased N-deposition [5].

At the biochemical level Rubisco is the key enzyme in the Calvin cycle (see Section S2), responsible for photosynthetic CO_2-fixation, and is considered the most abundant protein of the biosphere [6]. Considering the extensive literature dealing with the rate of photosynthetic carbon assimilation [7,8], plant growth and biomass production [9], the main focus of this review is to provide as complete a framework as possible of the mechanism of the Rubisco carboxylation reaction. Throughout the paper, particular attention is placed on

the structure and functioning of the active site as well on the functioning of the protein "molecular machine" including its physical molecular properties underlying CO_2 vs. O_2 selection. An overview of stepwise progresses achieved in elucidation of the carboxylase reaction mechanism since 2008 is presented, including a very recent model proposed by the Gready's Group in 2020. Finally, recent advances revealing the existence of strong biochemical links between the C- and N-fixation processes by plants will be reported.

The review includes a short summary of the literature dealing with the Rubisco protein structure, with the aim of providing information needed for the subsequent description of the reaction mechanism.

2. The Rubisco Reactivity

The Rubisco enzyme (Ribulose-1,5-bisphosphate carboxylase/oxygenase, EC 4.1.1.39) is a promiscuous enzyme catalyzing both the carboxylation and oxygenation reactions of the ribulose-1,5-bisphosphate-enediolate (Scheme 1).

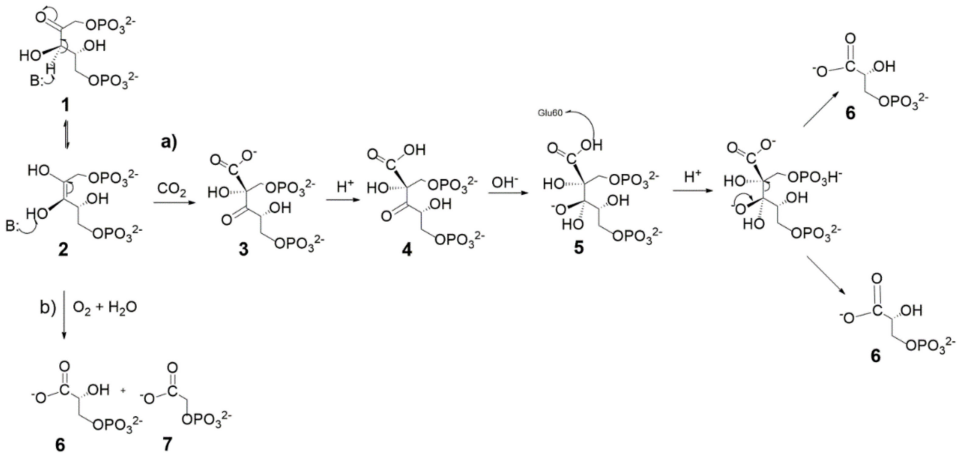

Scheme 1. RuBP conversion by Rubisco through the carboxylase (**a**) and the oxygenase (**b**) reactions. Following RuBP (**1**) enolization, the 2,3-enol(ate) intermediate (**2**) may react with CO_2 (**a**) or O_2 (**b**) co-substrates. The carboxylase reaction produces the 2-carboxy-3-keto-arabinitol 1,5-bisphosphate intermediate (**3**) undergoing protonation to the 2-carboxylic acid before hydration. The C2-C3-scission reaction in C3-gemdiolate (**5**) is described occurring in a concerted mechanism upon P1 protonation through a Grotthuss mechanism producing two molecules of 3-phospho-D-glycerate (3PGA, **6**). The oxygenase reaction produces 3-phospho-D-glycerate (3PGA, **6**) and 2-phosphoglycolate (2PG, **7**). (Previously unpublished scheme).

The carboxylase activity of the enzyme (Scheme 1a) allows for CO_2 fixation in photosynthetic organisms by converting D-ribulose-1,5-bisphosphate (RuBP) into two molecules of 3-phospho-D-glycerate (3PGA). The latter is subsequently reduced to D-glyceraldeyde 3-phosphate (G3P) within the Calvin-Benson-Bassham (CCB) cycle (see Scheme S1) [10]. Part of the G3P produced is further converted into hexose sugars. An analysis of the stoichiometry of the Calvin cycle shows that it takes six turns of the cycle (plus 12 moles of NADPH and 18 moles of ATP) to fix six moles of CO_2 into 1 mol of hexose sugar. As shown in Scheme 1a, the RuBP conversion proceeds stepwise encompassing enolization of RuBP followed by a carboxylation and hydration reactions to give, ultimately, two molecules of 3-phospho-D-glycerate. A detailed analysis of the reaction mechanism as well as a discussion of the energy profile of the overall reaction is reported in Section 8.

The oxygenase activity of the enzyme (Scheme 1b) produces 3-phospho-D-glycerate (3PGA) and 2-phosphoglycolate (2PG) by reaction of the 2,3-enediol(ate) intermediate with O_2. Due to the competition of CO_2 and O_2 for the Rubisco active site, the oxygenation reaction has been considered, for a long time, as a deleterious process with an overallnegative impact on CO_2-fixation [11]. However, very recently, this view has been criticized in the light of recent research progresses (see Section 10) [12].

3. The Rubisco's Secondary, Tertiary and Quaternary Structure

Due to the wide range of protein structures solved by X-ray crystallography and the availability of genomic and metabolomic data, four different Rubisco molecular isoforms have been identified in nature that essentially differ in the number of subunits and their arrangement within the macromolecular complex (Figure 1) [13].

Isoforms I and II, whose structural features are discussed in this section, play a central role in carbon fixation via the CBB cycle. The phylogenetic distribution of form I Rubisco encompasses all higher plants, red and brown algae, cyanobacteria and most chemoautotrophic bacteria while form II is found in photosynthetic bacteria and several methanogenic Archaea.

Mentioning briefly the remaining isoform of Rubisco proteins, form III Rubisco is found exclusively in Archaea and isoform IV (also named Rubisco-like protein, RLP) is found in both Bacteria and Archaea where it may have a role in sulfur metabolism.

This section analyzes the structural features of Rubisco proteins to provide a molecular basis for subsequent description of the carboxylase reaction mechanism. A detailed overview of the Rubisco's structure and function can be found in the review published by Andersson and Backlund in 2008 covering structures deposited to the PDB (Protein Data Bank) archive over approximately a 20-year period (including Rubisco-like proteins) [13]. Since 2008, several additional Rubisco structures have been solved by X-ray as, for example, the crystal structure of Rubisco from *Pisum sativum*, [14] *Galderia sulphuraria*, [15] *Rhodopseudomonas palustris* [16] and *Arabidopsis thaliana* [17].

The pioneering work published by Smith et al., in 1987 [18] describes Rubisco from *Nicotidiana tabacum* (form I Rubisco) as a globular protein, barrel-shaped ("a keg 105 Å along the 4-fold axis and 132 Å in diameter at the widest point of the keg"), showing a L_8S_8 quaternary structure where L denotes the "large" catalytic subunit and S denotes the "small" subunit (L: 52.9 kDa; S: 14.8 kDa). The eight L subunits are arranged as a toroid around a *z*-axis of four-fold symmetry. Along this axis a solvent channel transverses the molecular complex. The molecular symmetry of the L_8S_8 hexa-decamer of Rubisco from spinach is shown in Figure 1a [19]. Figure 1a is a view along the four-fold axis, while Figure 1b shows the protein viewed along one of the two-fold axes. In Figure 1b the two large subunits of the front-facing L_2 dimer are shown in yellow and blue color. The polypeptide chains of each L_2 dimer assume an antiparallel arrangement so that, the N-terminal domain of the yellow L subunit is close to the C-terminal domain of the blue L subunit.

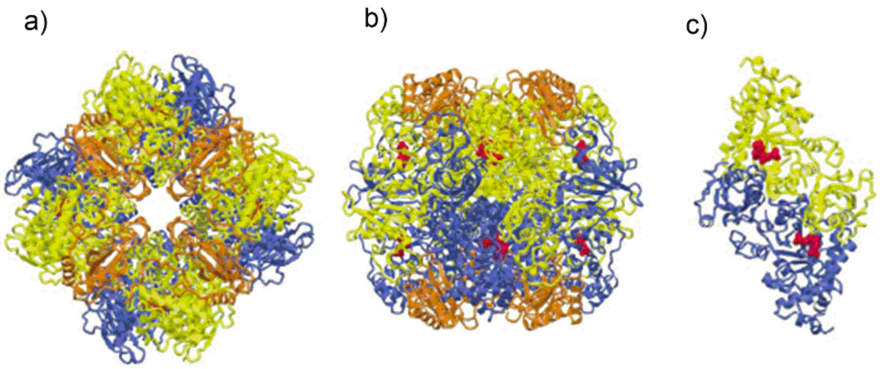

Figure 1. (**a**) Schematic drawing of Form I Rubisco from spinach showing the spatial arrangement of the L_8S_8 hexa-decamer view along the four-fold axis. The L subunits appearing in the figure are represented in yellow and blue. The figure also evidences the S subunits (represented in orange) delimiting the solvent channel; (**b**) schematic drawing of the Rubisco from spinach, view along one of the two-fold axes; (**c**) Form II Rubisco from *Rhodospirillum rubrum* showing the two-fold symmetry of the L2 dimer. The substrate mimic 2-carboxy-D-arabinitol 1,5-bisphosphate (2CABP), displayed as red spheres (Figure from ref. [19], adapted and used by permission of Elsevier (copyright © 2003).

Figure 1a,b also show the arrangement of the S subunits (represented in orange) clustered around the four-fold axis. Figure 1c represents a schematic drawing of the quaternary structure of type II Rubisco from *Rhodospirillum rubrum* consisting of a L_2 dimer [19].

The secondary structure elements (α-helices, β-strands and loops) of the polypeptide chain of Rubisco from spinach are shown in the connectivity diagram reported in Scheme S2 [20]. Interestingly, despite differences in the primary structure of different Rubisco proteins, the secondary structure of L subunits is highly conserved in the phylogenetic tree of the enzyme including isoforms I–III and Rubisco-like proteins (form IV).

As the protein secondary structure dictates the subsequent tertiary fold, a cartoon representation of the tertiary folding of Rubisco from *Arabidopsis thaliana* (form I Rubisco) and *Chlorobium tepidum* (Rubisco-like protein) obtained from the X-ray crystal structure is shown in Figure 2 [17,21].

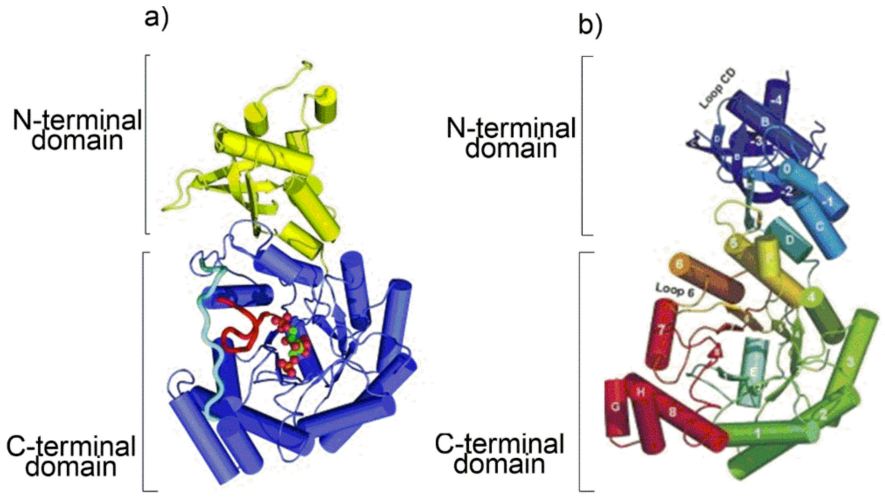

Figure 2. Tertiary structure folding of the L subunit of Rubisco from: (**a**) *Arabidopsis thaliana* (form I Rubisco); (**b**) *Chorobium tepidum* (Rubisco-like protein). One 2CABP molecule is shown bound at the active site of *Arabidopsis thaliana*. The figure evidences α-helices (as solid cylinders) and β-strands (as arrows) and the TIM-barrel unit at the C-terminal domain. Loop 6 is evidenced in red in both representations. Loop CD is also shown as a peculiarity of RLP (Figure 2a from ref. [17], used without changes from original source distributed under the CC-BY licence, http://scripts.iucr.org/cgi-bin/paper?S2059798317017132 (accessed on 25 June 2021). Figure 2b from ref. [21], adapted and used by permission of Elsevier (copyright © 2005).

At the C-terminal domain of each L subunit eight β-strands (from β1 to β8 in the topologic diagram shown in Figure S2) separated by eight α-helices (from α1 to α8) build up a very common tertiary fold currently named "TIM barrel" (TIM: triose phosphate isomerase). Interestingly, although RLP do not catalyze the RuBP carboxylation/oxygenation reactions, they share with the Rubisco enzymes substantial similarity in secondary and tertiary structure, probably because of a common archaeal ancestor.

More details about the quaternary structure of the L_2S_2 unit of *Galdieria sulphuraria* [15] Rubisco are shown in Figure 3. The L_2S_2 dimer is composed of two identical "head to tail" oriented L subunits viewed down the two-fold axis. The two S subunits are represented in blue.

As shown in Figure 3a,b, each L subunit hosts an active site which is located at the mouth of the TIM barrel. The N-terminal domain of the anti-paralleled L subunit in the L_2 dimer "covers" the TIM barrel contributing to the active site of the enzyme.

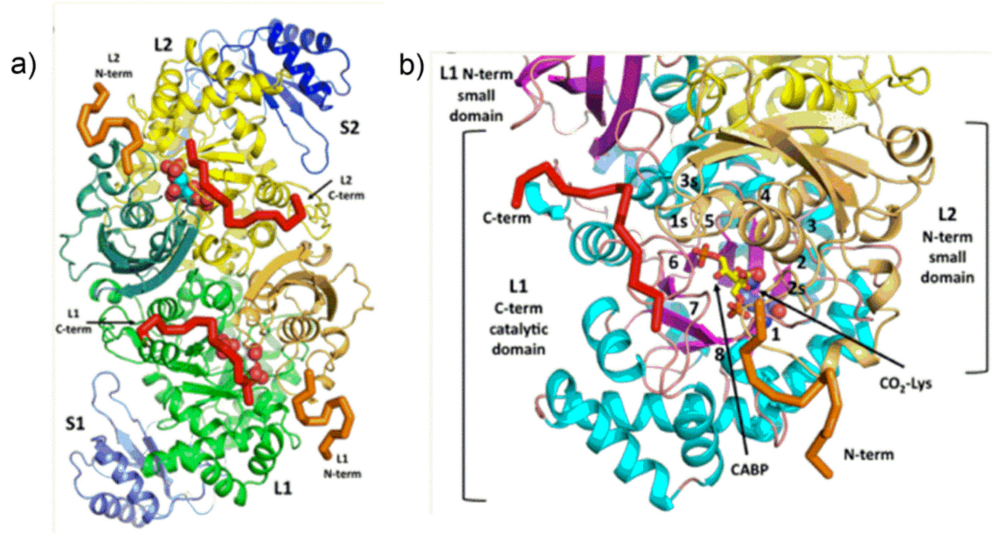

Figure 3. (**a**) Ribbon representation showing the quaternary structure of the L_2S_2 unit of Rubisco from *Galdieria sulphuraria* viewed down the two-fold axis. The two L subunits are represented in green (L1) and yellow (L2) with the highlighted N-terminal (orange) and C-terminal (red) regions. S1 and S2 subunits are represented in blue; (**b**) close-up of the L1 subunit (heavenly color) evidencing the TIM barrel domain. N- and C-terminal tails are marked in orange and red, respectively. Loop numbering is highlighted. N-terminal of the L2 subunit (L2 N-term small domain, represented in yellow color) is located at the mouth of the TIM barrel of the L1 subunit. Each L subunit guests one active site. In (**b**) the substrate mimic 2-carboxy-D-arabinitol 1,5-bisphosphate (2CABP) is shown as a bond-stick model and pointed by a black arrow. The CO_2-Lys201 residue is also pointed by a black arrow. (Figure from ref. [15], adapted and used by permission of PNAS (copyright © 2012).

The Rubisco Small Subunit

As the L subunit guests the enzyme active pocket, the S-subunit (ranging about 12–18 kDa among different Rubisco enzyme) is found only in form I Rubisco and is proposed to play both a structural and a functional role.

The primary structure for a series of S subunits from different organisms is reported in Figure S2 including the sequence of the secondary structure elements shown in ribbon representation in Figure S4 (orange ribbon) [22]. The figure evidences location of the βA-βB loop while the secondary structure elements of the L subunit functionally related to the S subunit are evidenced in green and yellow color. The βA-βB loop of each S subunit constitute an extension forming a β-hairpin. The βA-βB loops of four S subunits surround the opening of the solvent channel that transverses the L_8 octamer along the axis of four-fold symmetry (Figure 1a).

Structurally the S-subunit is involved in stabilizing the holoenzyme quaternary structure [23] and possibly modifying the conformation of the enzyme. In this respect, Hartl et al., have shown that the S subunit play a decisive role in assembly of the red-type Rubisco from *Rhodobacter sphaeroides* [24]. Concerning its functional role, the S-subunit is shown to affect several kinetic properties as the enzymatic catalytic efficiency and $S_{C/O}$ specificity (see Table S3). Moreover, Fukayama and co-workers have recently shown that overexpression of S subunit from C4 plants (*Pennisetum purpureum* and *Megathyrsus maximus*) in rice (a C3 plant) significantly enhances the k_{cat} value of the C3 Rubisco [25]. Analogously, expression of the small subunit of *Sorghum* (a C4 plant) in rice produces a Rubisco with higher catalytic rate when compared to rice [26]. Very recently Hanson et al., achieved expression of tobacco Rubisco in *E.coli* assembling enzyme complexes with different small subunits including a small subunit from trichome. The new technique allowed precise evaluation of the effects of different small subunits on the Rubisco kinetic parameters [27]. The Whitney group has produced new tobacco genotypes encoding both large and small subunits in

the chloroplast genome, producing a bioengineering chassis useful in evaluation of novel Rubisco complexes [28].

4. Mechanism of Enzyme Activation by Lys201-Carbamoylation

The information drawn from X-ray crystal structures and kinetic studies has allowed the proposal of a model describing the Rubisco physiological function as a sequence of "enzyme activation" and "enzyme catalysis" [29]. According to the model, the "enzyme activation" step consists in carbamylation of Lys201 affording an adduct stabilized by Mg^{2+} cation (ECM complex).

In particular, as depicted in Figure 4, the binding pocket of the unbound enzyme (represented as E) binds CO_2 (C) on Lys201 and the carbamylated-Lys201 is stabilized by the binding of Mg^{2+} (M) to give the ternary ECM complex Lys-201-NH-COO^- Mg^{2+}. This reaction allows the transition from a "catalytic inactive" to a "catalytic active" enzyme prone to tightly binds RuBP to give the ECMR complex. The ECMR complex may begin the "enzyme catalysis", reacting with CO_2 or O_2 according to the RuBP "carboxylation" or "oxygenation" reactions. Interestingly, it has been demonstrated that the "activating CO_2 molecule" (i.e., the CO_2 molecule binding Lys201) is not the CO_2 molecule involved in the RuBP carboxylation reaction (Scheme 1a).

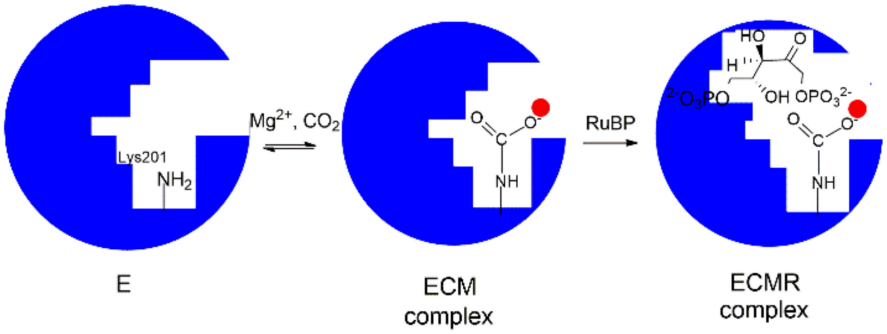

Figure 4. Schematic representation of the Rubisco "activation" and "catalytic" processes. E (representing the unbound enzyme) react with CO_2 (C) and Mg^{2+} (M) to form an active ternary complex (ECM) subsequently binding RuBP to give a quaternary ECMR complex. These events precede the carboxylation or oxygenation reaction (catalytic process) [29]. Previously unpublished figure.

The apparently "simple" Lys201-carbamylation reaction underlines a quite complex reaction mechanism recently disclosed by Stec [15]. The author succeeded in obtaining a high resolution structure (1.9 Å) of Rubisco from *Galdieria sulphuraria* bearing O_2 at the active site (in the center of the TIM barrel fold). Subsequently O2 was replaced by CO_2 by incubation of crystals at 40 °C in the presence of CO_2 and Mg^{2+}. After incubation, harvested crystals showed evidence of ECM complex formation. Comparison of the two crystal structures bearing O_2 or the Lys201-$CO_2^-$$Mg^{2+}$ complex allowed describing the structure of the "activation binding site" (Figure 5a) evidencing its different location with respect to the "catalytic binding site" described in the next section.

The proposed mechanism for the Lys201 carbamoylation reaction starts with a conformation change of His335 (comparing Figure 5a,b, note the conformational flexibility of the His335 side chain) allowing Mg^{2+} to locate in the transient binding site shown in Figure 5b. Interestingly, the metal ion was modelled to coordinate two OH^- groups, one water molecule and CO_2 (the latter in the end-on mode) displaying a pseudo-tetrahedral geometry with the linear CO_2 molecule pointing towards the ε-NH_3^+ group of Lys201. Subsequently, one metal-bound hydroxide promotes the proton abstraction of the ε-NH_3^+ group of Lys201 (see Figure 5c), producing the ε-NH_2 functionality prone to nucleophilic attack of the CO_2 molecule to give the ε-$NH_2^{(+)}$-$CO_2^{(-)}$ moiety. Finally, further proton abstraction from the ε-$NH_2^{(+)}$-$CO_2^{(-)}$ moiety produces the Mg^{2+}-stabilized aci-carbamate complex that relocates in a new binding site (shown in Figure 5d) where an octahedral

coordination sphere around Mg^{2+} is completed with Glu213 and Asp212 (not shown in Figure 5d). Relocation of the Mg^{2+}-complex allows His335-side chain return to its original conformation.

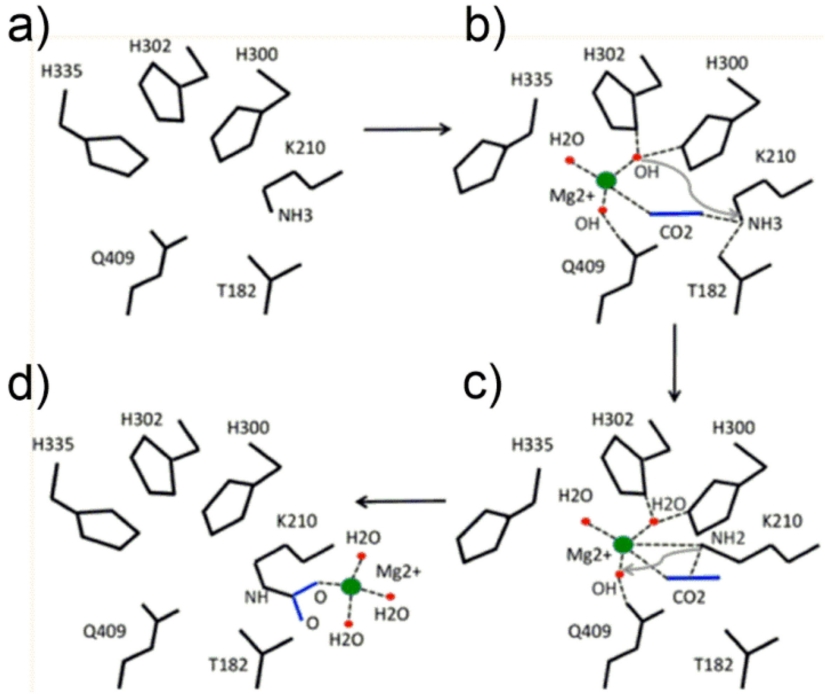

Figure 5. Mechanism of the Rubisco activation reaction as proposed by Stec. (**a**) Shows the arrangement of the His335 side chain contributing to the "activation binding site"; (**b**) shows that the His-335 side chain swings out to an alternative conformational state allowing a Mg^{2+} ion binding; (**c**) after proton abstraction, Lys201 swings in a position close to the CO_2-carbon affording the carbamylated-Lys201. The gray arrow shows the second OH^- group abstracting H^+ from the NH_2-carbamyl-moiety; (**d**) formation of a Mg^{2+}-stabilized aci-carbamate complex reaching a new location and prone to start the catalytic reactions (Figure from ref. [15], used by permission of PNAS (copyright © 2012)).

5. CO_2/O_2 Molecular Recognition Strategy

In the same study [15], Stec was able to propose a mechanistic explanation for the Rubisco ability to discriminate between CO_2 and O_2 at "RuBP-binding site". As intracellular (CO_2) is estimated approximately 7–8 μM in C3 plants and 80 μM in C4 plants, while [O_2] is about 260 μM, [30] a key point in Rubisco catalysis is the CO_2/O_2 competition for the RuBP-binding active site. To compensate for the low CO_2 intracellular level, Rubisco shows K_C values ranging from 8 to 19 μM and K_O values ranging from 230 to 620 μM while $S_{C/O}$ values range between 70 and 100 in plants (considering both C3 e C4 plants) and can reach values as high as 222 in *Galderia suphuraria* (a red algae).

Considering that Rubisco does not have specific binding sites for CO_2 or O_2 and the two gaseous molecules are not so different as far as dimensions and electrostatic potential surfaces are concerned (Figure 6a), the Rubisco higher specificity for CO_2 is not easily explained.

Stec [15] proposes that the two gaseous molecules "bind" to the same region of the active site, at the mouth of the TIM barrel, covered as a lid by the N-terminal domain of the adjacent L subunit (see Figure 3), where a high electrostatic field gradient is set up by the closeness of negative and positive surfaces potential. Figure 6b shows a negative surface potential (represented in red) at the N-terminal domain and a positively charged cavity (represented in blue) at the C-terminal domain. As the quadrupole moment of CO_2 is approximately 15-fold higher than that of O_2 (for CO_2 Qzz = −3.239 e a_0^2, for O_2 Qzz = −0.232 e a_0^2 as calculated by Stec), the quadrupole moment of the two gaseous

ligands interacting with the very strong electric field built across the active site allows discrimination between the two species.

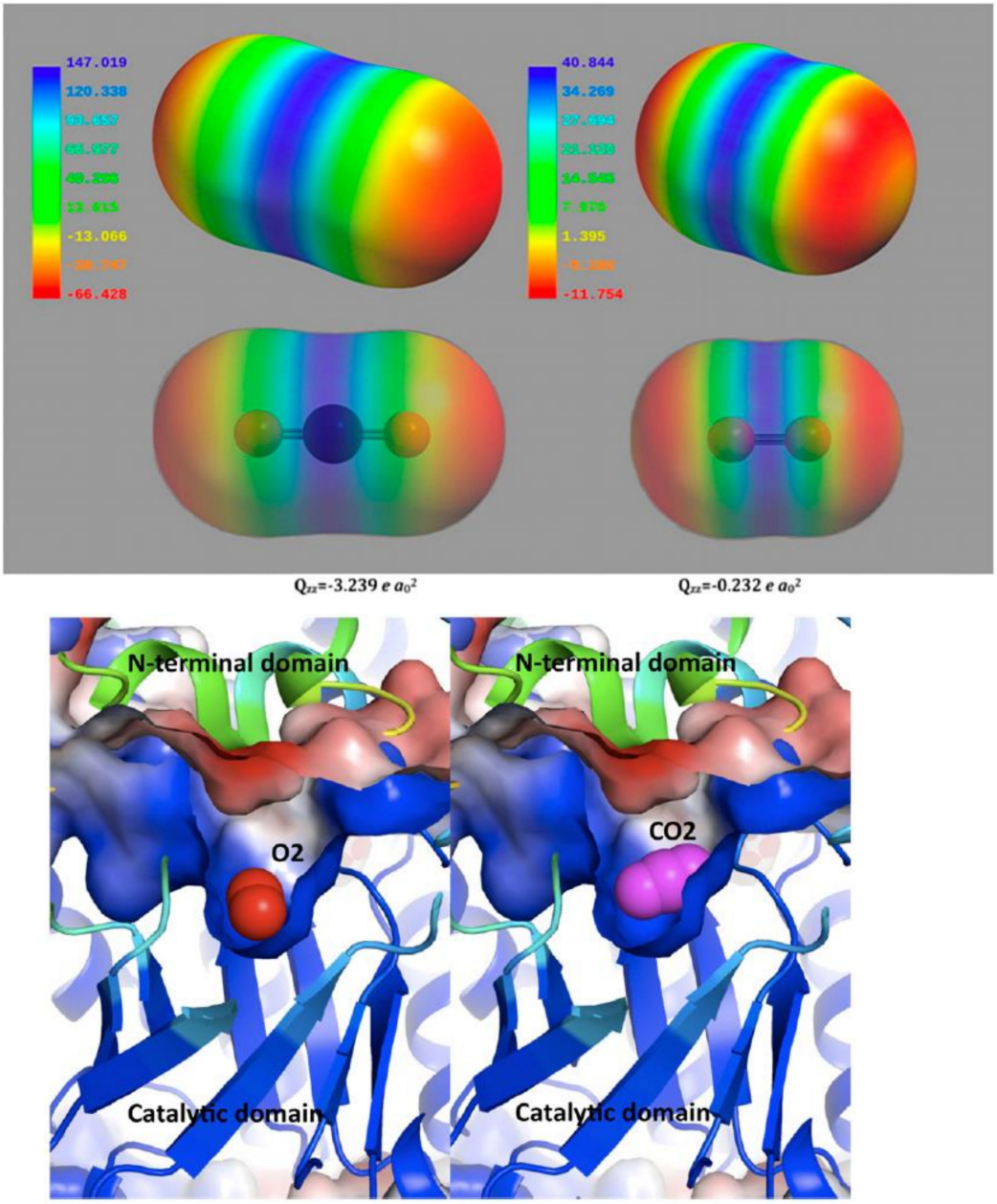

Figure 6. (**a**) Computed electrostatic potential molecular surfaces of CO_2 (left) and O_2 (right). The color scheme follows commonly accepted conventions: blue, positive; red, negative. The value of the Qzz component of the quadrupole moment, as calculated by Stec, is -3.239 e a_0^2 for CO_2 and -0.232 e a_0^2 for O_2; (**b**) a ribbon representation of the catalytic domain with bound gaseous ligands and surfaces colored by the electrostatic potential. O_2 (in red) and CO_2 (in purple) lie in a positively charged cavity (blue) of the TIM barrel. (Figure from ref. [15], used by permission of PNAS (copyright © 2012)).

The hypothesis advanced by Stec appears correct and provided a rationale for the minimal requirement of a L_2 dimer as a basic functional unit found across the Rubisco protein family. In fact, contact between the surfaces of the two subunits (facing each other) is needed to build up the gradient of the electric potential.

Andersson et al. [31] have also faced the problem concerning the favourable competition of CO_2 vs. O_2 by investigating, via molecular dynamics simulations, the interaction of the two gaseous molecules with the protein. A modelled L_8S_8 hexa-decamer was sol-

vated in a dodecahedron cell with an edge length of 12 nm and the desired amount of gas molecules was created to model the CO_2 and O_2 migration around the protein. The L_8S_8 models reproduced the protein structure of Rubisco from spinach (PDB access code 1aus, 1ruc and 1rcx) and from *Chlamidomonas reinhardtii* (PDB access code 1gk8). On the basis of the partition of the two gases between the protein and the surrounding solution, the authors were able to calculate the intrinsic affinity of Rubisco for CO_2 as +0.3 kJ/mol compared to +10 kJ/mol calculated for O_2. These data indicate that the whole protein binds CO_2 stronger that O_2. In agreement with Stec, the authors support the stronger CO_2 protein-binding with the difference in molecular quadrupoles of the two ligands. Moreover, by modelling the CO_2 and O_2 densities around the active site of Rubisco from *Clamidomonas reinhardtii,* the authors found that CO_2 has a preference for binding a region around the active site that extends to the closest S subunit (Figure S4). The simulation showed that the overall S subunit has a higher affinity for CO_2 than the overall L subunit suggesting that the S subunit plays a role as "CO_2 reservoir" for catalysis.

The hypothesis advanced by Stec is supported to some degree by a recent study by Falkowsky et al. [32] which analyzed the high resolution crystal structures of 11 Rubisco proteins stored in the PDB. The structural study was integrated with a phylogenetic analysis constructed using 55 Rubisco proteins sequences that confirmed that Rubisco homologs are assigned into four different phyletic groups named G-I, G-II, GIII and G-IV (the four forms are usually designated as form I, II, III and IV as mentioned in Section 3). Moreover the study demonstrated that: (i) G-II enzymes evolved from proteobacteria; (ii) G-III Rubisco evolved from the archaeal domain; (iii) G-I Rubisco evolved later being represented among bacteria, eukaryotic algae and higher plants. Distinct subclass of Rubisco proteins were found among the G-I group (i.e., IA, IB, IC and ID) showing a wide range of $S_{C/O}$ values ranging from 40 to 110.

The 11 high resolution crystal structures belonging to the monophyletic groups G-I and G-II allowed the observation that amino acid residues proximal to the active sites are not strictly conserved among different homologs and are likely sites for evolution. Crystal structures assigned the PBD ID5MAC, 1BXN and 4FOK are related to G-II, G-IC and G-ID Rubisco respectively, and belong to proteins progressively adapted to increasing O_2 concentration. Interestingly, comparison of these crystal structures evidenced the presence of higher surface charge potential proximal to the active site and solvent accessible channels connecting the protein surface to the active site. Enzymes bearing these larger positive channels easily "drive" CO_2 towards the active site, thanks to the electrostatic steering with the CO_2 quadrupole coming from a partial negative charge on the two oxygen atoms.

Most important is that the extension of the positive charged areas progressively increases from 5MAC to 1BXN structures reaching the maximum extension in the 4FOK structure. Interestingly, increasing extension of the positive charged areas within the three proteins parallels increased $S_{C/O}$ selectivity.

6. Structure of the Rubisco "Catalytic Active Site"

The inspection of the list of Rubisco's structure published by Andersson and Backlund in 2008 [13] evidences that a majority of the structural studies have dealt with Rubisco in complex with RuBP and Ca^{2+} [33] or in complex with 2CABP or XuRB (Scheme 2) and Mg^{2+}. Only one crystal structure of Rubisco in complex with RuBP and the Mg^{2+} ion has been solved, probably because of an inherent instability of the RuBP-Mg^{2+}-protein complex [34]. By contrast, 2-carboxy-D-arabinitol-1,5-bisphosphate (2CABP) forms with the Mg^{2+} ion an exchange-resistant complex which turned out to be useful in crystallographic studies [35].

The structure of 2-carboxy-D-arabinitol-1,5-bisphosphate (2CABP) shown in Scheme 2 closely resembles the six-carbon intermediate 2-carboxy-3-keto-D-arabinitol-1,5-bisphosphate (3-keto-2-CABP) assumed to be the transient intermediate in the carboxylation reaction. Therefore, for a long time it was considered that the interaction of 2CABP with Mg^{2+} mimics the transition state of the metal-bound β-keto acid intermediate.

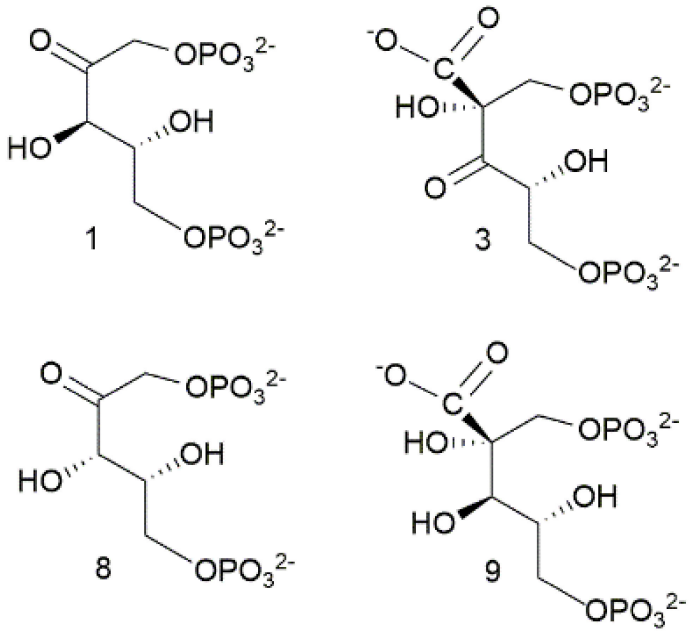

Scheme 2. Structure of: D-ribulose-1,5-bisphosphate (RuBP, **1**), 2-carboxy-3-keto-arabinitol- 1,5-bisphosphate (3-keto-2-CABP, **3**); D-xylulose-1,5-bisphosphate (XuBP, **8**); 2-carboxy-D-arabinitol-1,5-bisphosphate (2CABP, **9**). (Previously unpublished scheme).

Two capstone publications reporting the structure of Rubisco from spinach in complex with 2-carboxyarabinitol-bisphosphate (2CABP) are those of Knight et al., in 1990 [36] and Anderson et al., in 1996 (PDB code number 8ruc) [35]. The two structures were resolved at 2.4 and 1.6 Å, respectively. As amino acids taking part in catalysis are often directly involved in substrate interactions, a distance <4.0 Å between amino acid residues and 2CABP was used to identify amino acids as catalytically competent.

As shown in Table 1 [36], amino acids contributing to the catalytic pocket of Rubisco are located at the loops following the C-terminal ends of the β-strands (from β1 to β8 of the C-terminal domain) and at the N-terminal domain of the antiparallel L subunit. Amino acid residues represented in bold are strongly conserved among Rubiscos from diverse species.

Table 1. A distance <4.0 Å between amino acid residues and 2CABP was used to identify amino acids which were catalytically competent. The list denotes amino acids located at the C-terminal end of the αβ-barrel of L1 subunit and at the N-terminal end of the antiparallel L2 subunit. Amino acid residues represented in bold are strongly conserved among Rubisco proteins (Table from ref. [36], used by permission of Elsevier (copyright © 1990)).

Loop	Amino Acid	Loop	Amino Acid
	Thr173	Loop 7 (C-terminal domain)	**Ser379**
Loop 1 (C-terminal domain)	**Lys175**	Loop 7 (C-terminal domain)	Gly380
Loop 1 (C-terminal domain)	**Lys177**	Loop 7 (C-terminal domain)	Gly381
Loop 2 (C-terminal domain)	**Lys201**	Loop 8 (C-terminal domain)	Gly403
Loop 2 (C-terminal domain)	**Asp203**	Loop 8 (C-terminal domain)	Gly404
Loop 2 (C-terminal domain)	**Glu204**		
Loop 5 (C-terminal domain)	**His294**	LoopA (N-terminal domain)	**Glu60**
Loop 5 (C-terminal domain)	**Arg295**	(N-terminal domain)	Thr65
Loop 6 (C-terminal domain)	**His327**	(N-terminal domain)	Trp66
Loop 6 (C-terminal domain)	Lys334	LoopB(N-terminal domain)	**Asn123**
Loop 6 (C-terminal domain)	Leu335		

Amino acids in bold characters are those conserved.

Figure 7 shows the structure of the active site of activated 2CABP-bound Rubisco as proposed by Gready et al., in 2008 [37] (the structure has been plotted from the file 8RUC deposited at the Protein Data Bank, Anderson, 1996 [35]). According to this model, carbamylated Lys201 (KCX201), Asp203, Glu204, 2-carboxy-D-arabinitol-1,5-bisphosphate (2CABP) and H_2O complete the octahedral distorted geometry around Mg^{2+}.

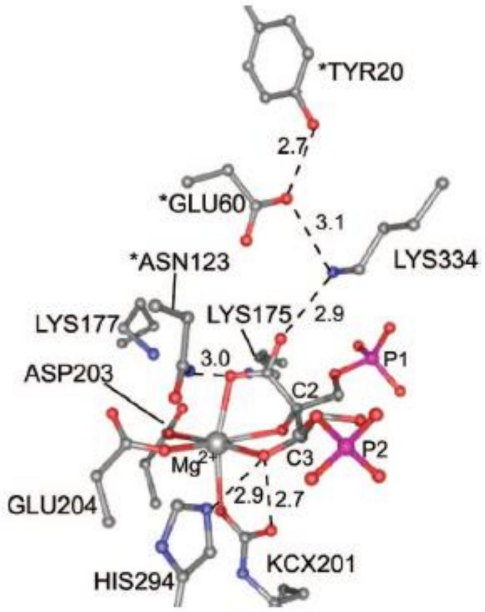

Figure 7. Structure of the active site of activated 2CABP-bound Rubisco plotted from the 8RUC.PDB file (Protein Data Bank) showing the coordination environment of Mg^{2+} as proposed by Gready et al., in 2008. Residues with an asterisk in the label are from N-terminal domain of the antiparallel L subunit. Numbering of amino acid residues is based on that of spinach Rubisco (Figure from ref. [37], adapted and used by permission of American Chemical Society (copyright © 2008).

Moreover, Figure 7 evidences Asn123, Glu60 and Tyr20 residues (marked with an asterisk), located at loopA and loopB of the N-terminal domain of the L-partner subunit, interacting with the ligands of the first coordination sphere. Lys334 is an amino acid residue of loop 6 (i.e., the loop connecting β-strand 6 with α-helix 6 of the TIM barrel) undergoing conformational changes during catalysis (see Section 7).

Concerning the binding of the actual RuBP ligand to Rubisco, the crystal structure resolved by Andersson in 1997 [33] (refined to 2.1 Å) contained the catalytically inactive Ca^{2+} interacting with the sugar phosphate. RuBP is proposed to bind the metal ion through the O_2 and O_3 to give a five-member metallacycle. This structure has been considered by several authors as the starting structure to model the mechanism of the carboxylation reaction (see Section 8).

7. Conformational Changes during Catalysis: "Open" and "Closed" Form of the Enzyme

In an interesting study Curmi et al. [38] have compared X-ray crystal structures of Rubisco from spinach, tobacco and *Synecococcus* considering either "empty active site" proteins (i.e., polypeptides bearing the ECM complex but lacking substrate binding) and sugar phosphate-bound forms of Rubisco (including RuBP, 2CABP or XuBP ligands). Careful comparison of structures allowed identification of a complex sequence of conformational changes occurring during transition from the so called "open" (with the active site accessible to solvent) to "closed" states of the protein. Occurrence of catalysis requires the enzyme to lie in the "closed" state with the active site not accessible to the solvent.

After enzyme activation (i.e., ECM-complex formation as described in Section 4) Rubisco remains in an "open" conformation schematically depicted in Figure 8a. Figure 8a (open state) shows a view from the central axis of the TIM barrel of the L1-subunit (referred

as "active site exposed") which is partially "covered" by the N-terminal domain of the juxtaposed L2 subunit. In the "open state", Figure 8a shows loop 6 is in a retracted position, and shows the C-terminal helical domain (composed of amino acid residues from Trp462 to the C-terminus) pointing far from the active site.

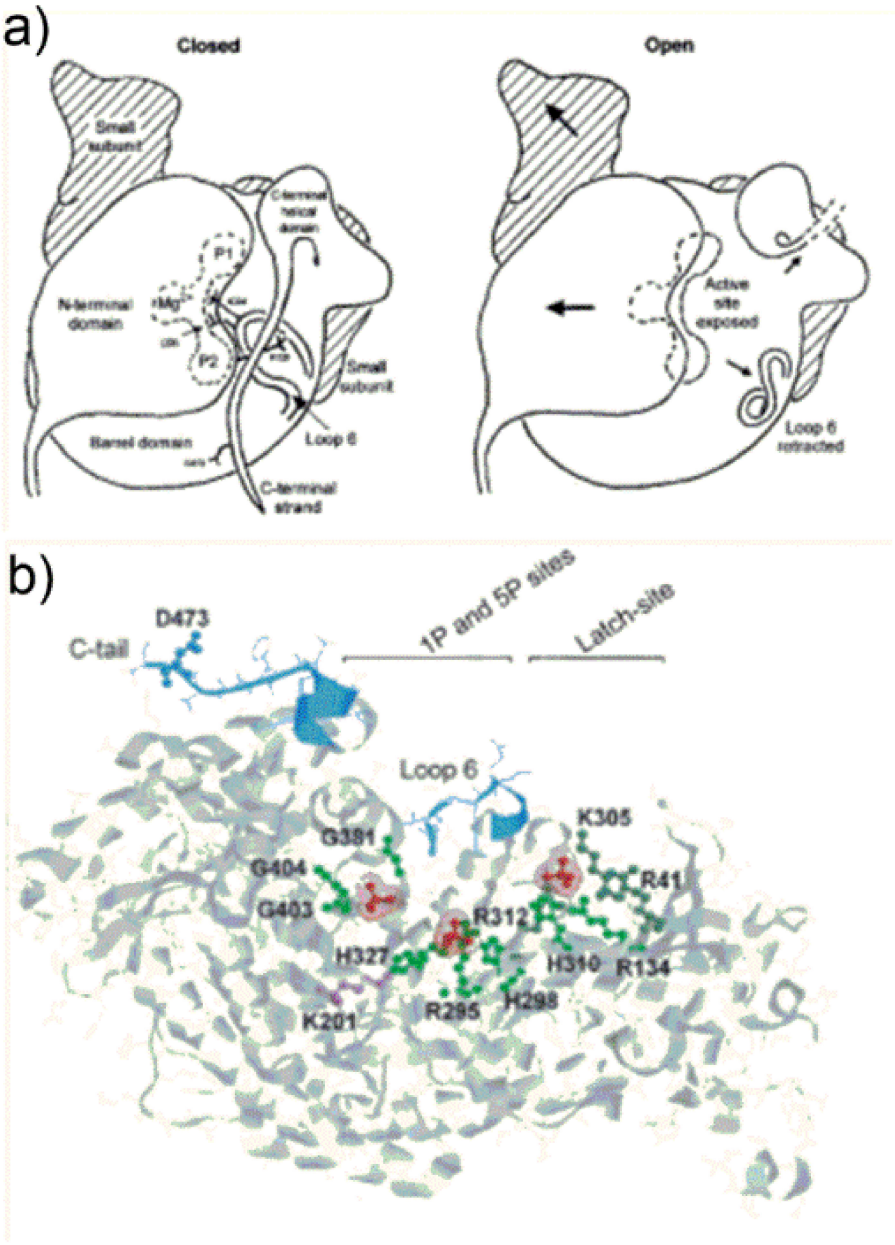

Figure 8. (**a**) Schematic illustration of the "open" to "closed" state transition of the catalytic site of Rubisco. The "open" to "closed" transition occurs through a sequence of three main conformational changes; (**b**) evidences the binding sites for 1P- and 5P-groups of RuBP (in red) in Rubisco from the cyanobacterium *Synechocystis* sp. The third phosphate group shown (in the latch-site) is assigned a particular role in the regulation of catalysis (Figure 8a from ref. [38], used by permission of Elsevier (copyright 2000); Figure 8b from ref. [39], adapted and used by permission of American Society of Microbiology (copyright © 2005)).

Once RuBP binds tightly to the active site, the enzyme transits from the "open" to the "closed" conformation shown in Figure 8a. The catalytic site is schematized evidencing location of the Mg^{2+} as well as the P1- and P2-binding sites of the sugar phosphates.

The "open" to "closed" transition occurs through a sequence of three main conformational changes: (i) first the N-terminal domain of the L subunit rotates as a semi-rigid body occluding the entrance of the TIM barrel (i.e., the sugar phosphates binding pocket); (ii) loop 6 extends in a position that occludes the active site; (iii) the C-terminal strand overlaps with loop 6.

It is worth noting that "open" state conformation is also observed in X-ray crystal structures of proteins bearing 2CABP bound to the inactivated (metal-free) active site or RuBP bound to the catalytically inert Ca^{2+}. In the latter cases, sugar phosphates bind the active site quite weakly.

Taking a closer look at the tertiary structure conformational changes occurring during open-to-closed transition, Curmi et al., propose that a central role is played by binding of the two phosphate anions of ribulose-1,5-bisphosphate to specific active site positions. A very important point noted by Curmi et al., is that all Rubisco crystallized in the "closed" state show 1P and 5P at a distance less than 9.1 Å, while all proteins crystallized in the "open" state show the two phosphates at a distance higher than 9.4 Å, pointing out that decrease of the 1P-5P distance triggers important conformational changes.

Figure 8b evidences in red the 1P- and 5P-group binding sites of RuBP in Rubisco from the cyanobacterium *Synechocystis* sp. [39]. In the "open" state, 1P binds the main-chain NH-groups of Gly381, Gly404 and Gly403 (located at β-strand-7 and loop-8 of the TIM barrel) and engages in hydrogen bonding with Trp66 located at the N-terminal domain of the antiparallel L-subunit (not shown in Figure 8b). The 5P-anion engages in hydrogen bonding with Arg295 and His298-H^+ occupying the so called "upper subsite" located at β-strand-5 of the TIM barrel. The third phosphate group shown in Figure 8b interacts with the latch-site which is assigned a particular role in regulation of catalysis.

During the open-to-closed transition the 5P-group displaces, occupying the so called "lower subsite" upon interaction with Arg295 and His327 (Figure 8b). Moreover, the 1P-anion reaches a position closer to the 5P-group engaging in hydrogen bonding with Thr65 of the N-terminal domain of the adjacent L2 subunit (not shown in Figure 8b). A change of the backbone ψ torsion angle of Thr65 moving towards the 1P-group seems to be the event triggering the rotation of the N-domain to cover the C-terminal domain TIM barrel. It is important to note that amino acid residues from Trp66 to Thr75 are located in the middle of the loop connecting α-helix-B to β-strand-C of the N-terminal domain (see Figure S2). This loop constitutes the major interface between the N-terminal domain of one L subunit and the TIM-barrel of the antiparallel L subunit and does not alter in position relative to the TIM barrel during open-to-closed transition. In contrast, the remainder of the N-terminal subunit is triggered to rotate.

Conformational changes occurring at loop 6 enable loop mobility between two well defined states i.e., "retracted" (while the enzyme is "open state") and "extended" (while the enzyme is "closed state"): extension of loop 6 over the active site (to reach the enzyme closed state) is due to dramatic changes in the φ and ψ angles of Gly333 and Gly337. These residues provide two flexible elements favoring the rearrangement. Moreover, the 5P-anion binding to the "upper sub-site" exerts steric hindrance toward Leu335 of loop 6 favoring the "retracted" vs. "extended" conformation of the loop.

As the enzyme needs to reach the "closed state" before initiating the carboxylation/oxygenation reactions, conformational changes significantly affect the "entropic cost" of enzyme functioning. Stec points out that the required conformational changes may explain, in part, the Rubisco's low catalytic turnover rates. Moreover, Gready et al. [37] point out the low $k_{cat,C}$ of Rubisco enzymes may be due to the complexity of the reaction mechanism with all reaction steps taking place at a single active site. The following section will focus on the description of the reaction mechanism as recently proposed by Gready's research group.

8. Mechanism of the Rubisco Carboxylation Reaction: The Role of Broensted Acid-Base Catalysis

By integrating information from the body of existing literature concerning crystallographic and mutational studies, Cleland et al., proposed in 1998 the first consensus mechanism for the Rubisco carboxylase reaction [40]. The model encompasses RuBP-enediolate coordination to the Mg^{2+} ion undergoing subsequent transformation implying, in specific steps, proton-transfer reactions and water addition.

From this study it became clear that elucidation of the Rubisco carboxylation mechanism requires large reliance on computational methods, as elementary steps consisting in proton exchanges and water addition cannot be disclosed by analysis of X-ray crystal structures. A decade later, Gready et al. [37] were able to propose a detailed reaction mechanism for the Rubisco carboxylase reaction by integrating computational studies with a density functional theory calculation on active-site fragment models. To allow DFT analysis, active site fragment models of a size of up to 77 atoms were built by using the coordinates of Rubisco crystal structures. In particular the authors have used the crystal structure of the activated spinach Rubisco complexed with Ca^{2+} and RuBP (PDB code number 1RXO [33] showing Ca^{2+} coordination as depicted in Figure 9) and that of spinach Rubisco complexed with Mg^{2+} and 2CABP (PDB code number 8RUC [35]). The building of approximately twenty fragment models enabled mapping of structures of reaction intermediates, and the computational analysis (based on the use of the B3LYP functional) allowed optimizing of their geometries. Validation of the optimized model structures was carried out comparing calculated interatomic distances with the active-site structures revealed by X-ray diffraction. For 75% of the compared distances, deviation of less than 0.6 Å was obtained.

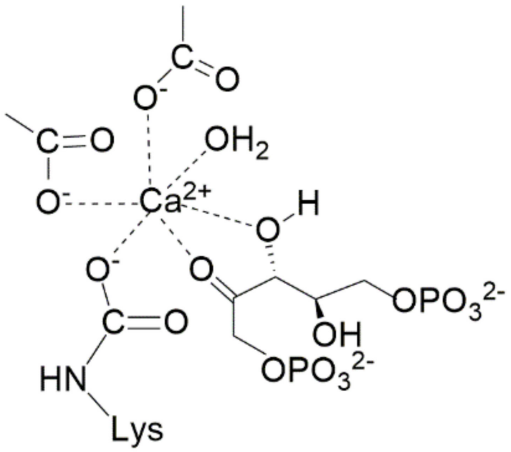

Figure 9. Structure of the active site of activated RuBP-bound Rubisco plotted from the 1RXO PDB file (Protein Data Bank) showing the coordination environment of Ca^{2+}. (Figure 9 from ref. [33], adapted and used by permission of Elsevier (copyright © 1997)).

Relevant features of the reaction mechanism as proposed by Gready et al., in 2008 [37] are shown in Figure 10 (amino acid sequence numbering refers to Rubisco from spinach). The initial model fragment along the reaction coordinate shown in Figure 10 was modelled using the active site structure shown in Figure 9, but replacing Ca^{2+} with Mg^{2+}. However, Figure 10 does not show the pseudo-octahedral coordination around Mg^{2+} as, for a simplified view, only the RuBP ligand and the water molecule (H_{w1}-O_w-H_{w2}) are highlighted. According to Gready's description, every single step of the reaction involves proton-transfer process. Therefore, amino acid residues acting as Lewis base are highlighted in blue boxes, while amino acid residues stabilizing anions (or the negative charge of dipolar groups) through hydrogen bond are shown in red boxes.

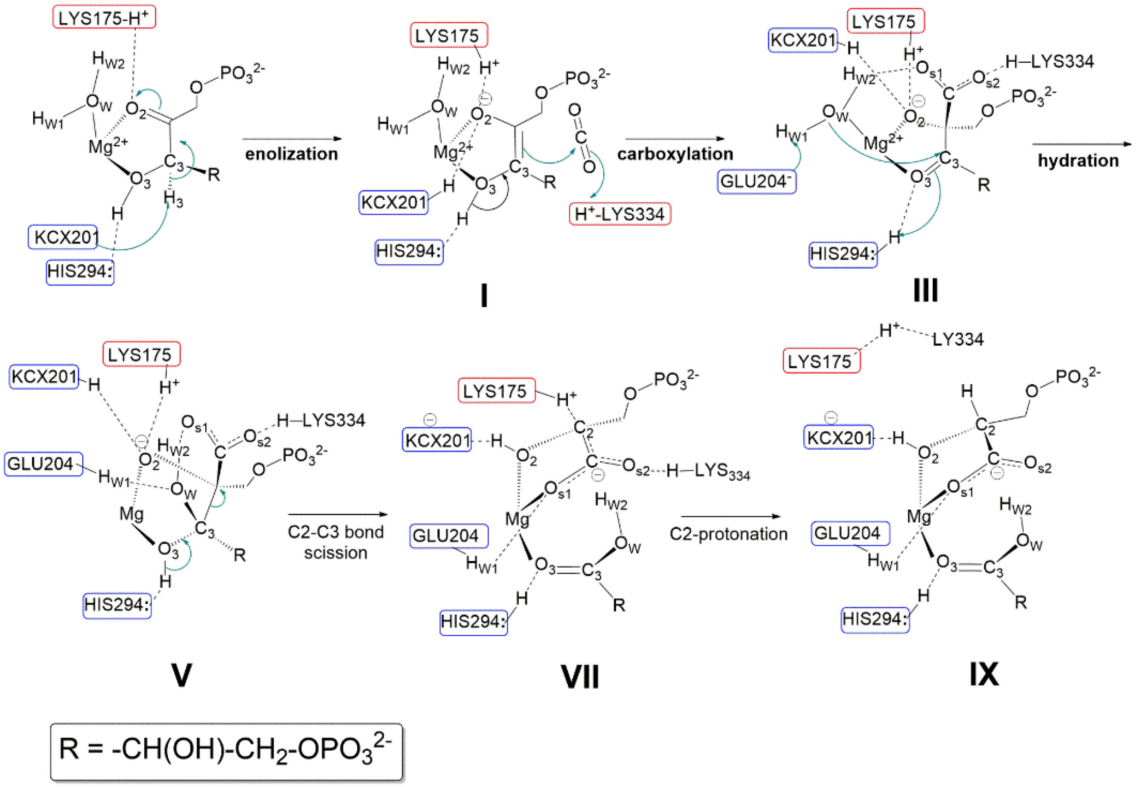

Figure 10. Proposed reaction mechanism for the conversion of RuBP at the Rubisco catalytic site. Amino acid residues acting as Lewis base are highlighted in blue boxes, while amino acid residues stabilizing anions through hydrogen bond are highlighted in red boxes. Numbering (I–IX) refers to geometries of local minima along the reaction pathway obtained using Gready's theoretical model. (Figure from ref. [37], adapted and used by permission of American Chemical Society (copyright © 2008)).

Relevant steps involving acid-base catalysis are summarized below:

(1) Enolization step: Following RuBP binding to Mg^{2+} through O2 and O3, Lys175-H^+ is proposed to engage in hydrogen bonding with the carbonyl C2=O2. The carbamoyl moiety Lys201-COO^- (also noted as KCX201) acts as a base abstracting the C3-H3 proton allowing RuBP enolization to the 2,3-*cis*-enediol(ate) form (shown in structure I). Both KCX201-H and LYS175-H^+ are proposed to engage in hydrogen bonding with O2 partially neutralizing its negative charge. His294 is proposed to play an important role in RuBP enolization, engaging in hydrogen bonding with H-O3 and preventing, thus, its interaction with $KCX201^-$. As a matter of fact, it is assumed that in the absence of the His294-H-O3 interaction the carbamoyl group would abstract H-O3 more easily than H3-C3.

(2) Carboxylation step: following RuBP enolization, His294 is proposed to abstract the H3-O3 proton allowing ketonisation at C3 followed by negative charge localisation at C2 (structure I). The *Si* face of the incipient C2-carbanion attacks CO_2 forming the 2-carboxy-3-keto-D-arabinitol-1,5-bisphophate intermediate. Structure III evidences the hydrogen-bonding network, stabilizing the geometry of the carboxylate intermediate within the fragment model. Relevant interactions are: (i) the protonated Lys334-H^+ and the water molecule stabilise the negative charge of the carboxylate moiety; (ii) His294-H^+ maintains hydrogen bonding with O3; (iii) Lys175-H^+ and KCX201-H keep in hydrogen bonding with O2 atom.

(3) Hydration step: to start the hydration step (structure III) H_{w1} is proposed to be abstracted by $Glu204^-$ anion allowing nucleophilic attack by OH^- onto the C3 carbon. His294-H^+ assists the hydration reaction by proton transfer to O3 allowing C3 to reach a sp^3-hybridization to form a six-carbon gem-diolate intermediate (see structure V).

(4) C2-C3 bond scission and C2 protonation: Structure V shows the six-carbon gem-diolate intermediate which is proposed to undergo proton abstraction from H-O3 by His294 with ketonization at the C3 carbon followed by C2-C3 bond scission. As a consequence two molecular fragments are produced:(i) one 3-phospho-D-glyceric acid molecule (lower part of the structure); (ii) a C2-carbanion that delocalizes the negative charge over the carboxylate moiety producing an aci-acid intermediate (it is important to note that the C2=$CO_{s1}O_{s2}^-$ fragment is planar), and this charge is stabilized by Lys334-H^+ and Lys175-H^+ (see structure VII). Finally Lys175-H^+ promotes stereospecific protonation of the C2 carbanion to yield the 3-phospho-D-glycerate. Only at this stage does Lys334-H^+ engage in hydrogen bonding with Lys175.

The Rubisco reaction model summarized in Figure 10 has been "reshaped" by using recently available computational methods (as hybrid semi-empirical (SE) quantum mechanics, molecular mechanics (QM/MM) plus molecular dynamics (MD) calculations (QN/MM + MD)] in conjunction with energy-minimization calculations. The new computational methods allowed the building of active-site fragment models (FM21 shown in Figure 11) consisting of many hundreds of atoms [35]. FM21 was built based on coordinates from the crystal structure of spinach (PDB code 8RUC, [29]) and includes 343 atoms within a range of 24 Å from Mg^{2+}.

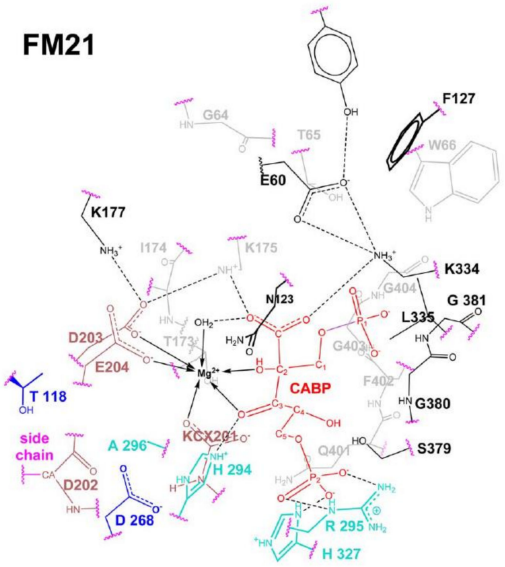

Figure 11. Structure of the FM21 model consisting of 339-342 atoms around the Mg^{2+} cation. Where residues overlap visually, residues at the back are shown in gray and residues at the front are shown in thick black lines. Truncations from enzyme are highlighted as wavy lines in magenta. Only one water molecule coordinated to Mg^{2+} is shown. (Figure 11 from ref. [41], used by permission of John Wiley and Sons (copyright © 2018)).

The new study [41] does not consider the RuBP enolization step but focuses on the subsequent elementary steps of the reaction coordinate (i.e., carboxylation, hydration, C2-C3 bond scission and C-2 protonation) shown in Figure 12.

Results of the study [41] provide new insight into the following reaction steps which confirm the relevance of the acid-base chemistry: (i) the 2-carboxy-3-keto-arabinitol-1,5-diphosphate (3 in Figure 12) was shown to undergo protonation at the carboxylic group (affording the C2-carboxylic acid) to energetically facilitate the subsequent nucleophilic attack of OH^- onto the C3 carbon leading the C3-gemdiolate 5; (ii) the C3-gemdiolate was found to the most stable intermediate bound to the Mg^{2+}-cation along the reaction coordinate, as shown from Relative Potential Energy calculations; (iii) the C2-C3 scission/C2-protonation events were described occurring in a concerted mechanism; (iv) Lys175-H^+ was established acting as proton source in step (iii).

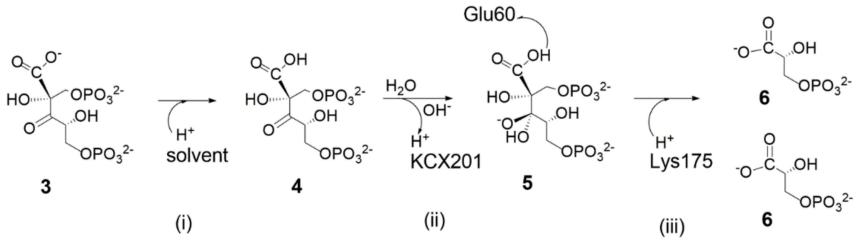

Figure 12. Mechanism for the steps following C2-carboxylate formation: (**i**) C2-carboxylic acid is formed by protonation from an unknown donor via solvent channels; (**ii**) C3-gemdiolate is formed as H_2O approaches C3 and undergoes proton abstraction by KCX201; (**iii**) C2-C3 bond scission of the C3-gemdiolate, concerted with stereospecific C2-protonation by LYS175 and deprotonation of the C2-carboxylic acid by GLU60, yields product. (Figure 12 from ref. [41], adapted and used by permission of John Wiley and Sons (copyright © 2018)).

It is worth noting that all the previously proposed reaction mechanisms have considered a two-step reaction consisting in the cleavage of the C2-C3 carbon bond, affording a C2-carbanion intermediate followed by stereospecific C2-carbon protonation to give 3-phospho-D-glycerate.

Due to the novelty of the conclusion drawn in the previous work concerning the C2-C3 scission/C2-protonation steps occurring in a concerted mechanism, a more careful investigation was developed by Gready et al., in 2019 [42] by applying ab initio molecular dynamic simulations on the molecular fragment FM21 (Figure 11 by using the Kohn-Sham density functional theory (Figure 13b).

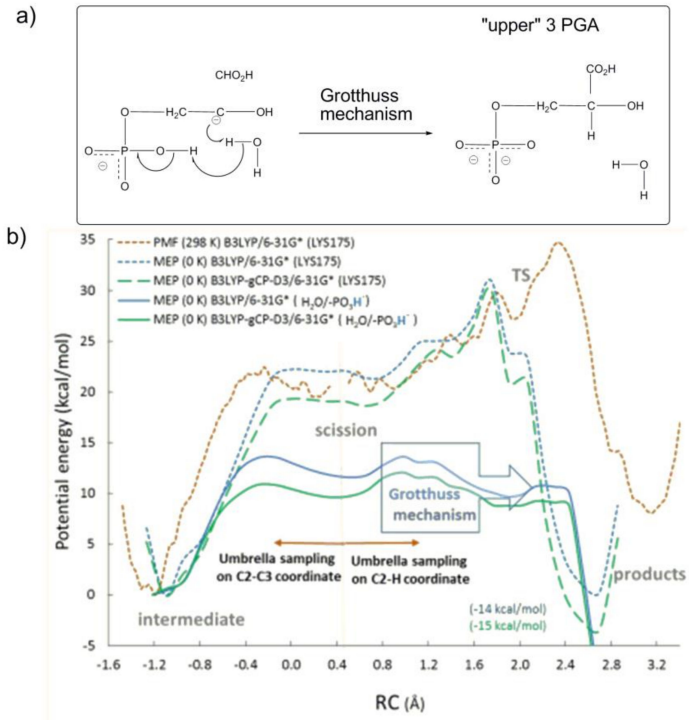

Figure 13. (**a**) Mechanism of the C2-protonation steps occurring in a concerted mechanism, as proposed by Gready et al., in 2019; (**b**) MEP (0 K) and PMF (298 K) plotted against the reaction coordinate (RC) defined as the difference between C2-C3 and C2-H distances. The C3-gemdiolate shown in Figure 12 is named "intermediate". 3PGA is named "products". The legend shows the density functional used for energy calculation and the proton donor moiety for each reaction profile is indicated in parenthesis (either protonation directly from Lys175-H^+ or via the Grotthuss mechanism initiated by a phosphate proton and a single water molecule. Proton is highlighted in blue). (Figure 13 from ref. [42], adapted and used by permission of American Chemical Society (copyright © 2019)).

By computing the variation of potential mean force (PMF at 298 K) and minimum potential energy (MPE at 0 K) along the reaction coordinate, the study intended to assess whether protonated Lys175-H^+ or a proton translocation across a network of H-bonded water molecules with P1-group as proton donor (the so called phosphate mediated Grotthus mechanism, Figure 13a) is involved in the stereospecific protonation of the C3-gemdiolate ("intermediate" in Figure 13b) to afford 3PGA ("products" in Figure 13b).

Interestingly, the computational study revealed that the protonation of the C3-gemdiolate from Lys175-H^+ (represented as the orange dotted line in Figure 13b) is not favoured, as products are located 5 kcal/mol higher than the C3-gemdiolate intermediate. In contrast, the proton transfer process occurring through the Grotthuss mechanism (represented as the blue and green continue lines in Figure 13b) shows an activation energy of 15.6 kcal/mol (in close agreement with experimental data) and obtains products 14 kcal/mol more stable with respect to C3-gemdiolate intermediate.

All of the studies carried by the Gready group summarized above indicate that the last reaction steps concerning C2−C3 scission (of the C3-gemdiolate) and stereospecific C2 protonation described in Figure 13a proceed through preliminary protonation of the P1-group of the C3-gemdiolate. Subsequently, in a concerted reaction mechanism, a proton at the P1-group induces stereospecific protonation of the C2-carbon via the Grotthuss mechanism.

Due to the rapidly evolving view of the Rubisco reaction mechanism, in a very recent publication, Cummins and Gready [43] have considered the reactional events from a completely new perspective.

The rationale behind the reaction mechanism proposed in Figure 10 is that RuBP strongly coordinates Mg^{2+} and most parts of the Brœnsted acid-base reactions imply "movement" of amino acid side chains approaching the substrate. As a consequence, the requirement for conformational chain reorganization implies a considerable amount of strain energy. In a very recent publication, Cummins and Gready [43] have refined the model of the Rubisco catalytic site using a complex of approximately 340 atoms, as in previous studies, but introducing new structural details. Considering that the structure of Rubisco from spinach (PDB 8RUC) gives a snapshot of the enzyme in its "closed" conformation, a careful analysis of the water molecules identified by X-ray crystallography around RuBP and Mg^{2+} suggests the formation of short water wires. The introduction of the "water wire" concept into the model allows proton transfer processes to occur through the Grotthuss mechanism (at several steps along the reaction coordinate) as an alternative to the previous amino acids side-chain conformation change mechanism. Notably, the new reaction model does not imply a direct coordination of RuBP to Mg^{2+}. Interestingly, the new model allows the calculation of accurate potential energy values for intermediates and transition states along the reaction coordinate by using the B3LYP/6-31G* and corresponding corrected B3LYP-gCP-D3 functional.

Figure 14a displays relevant structural features of the initial molecular complex (**A**) considered in the new model. Although the choice of molecular arrangement within the active site is somehow arbitrary, the authors consider this a logical choice based on the information available. Due to the complexity of the overall RuBP carboxylation reaction, only the enolization and carboxylation/hydration steps are analyzed here.

Relevant features of Figure 14a are: (i) Mg^{2+} is coordinated to the LYS201-carbamylate moiety (usually referred as KCX201) in the initial molecular complex A; (ii) two water molecules are shown engaging in a network of hydrogen bonding with KCX201 and RuBP in A; (iii) His294 is assumed to be unprotonated in the activated RuBP unbound active site, so that it can interact with O3-H once RuBP enters the active site to give the protonated form His294$^+$. Proton transfer processes required for RuBP enolization are mediated by two proton wires acting in sequence: H3-H_2O-KCX201 (see transition state $A^{\neq}$) and KCX201-H_2O-H_2O-O2 (see intermediate B). Enolization is started by assistance of the H3-H_2O-KCX201 proton wire acting in H3 abstraction to form H_3O^+ (in $A^{\neq}$) followed by H^+ transfer to KCX201 to give KCX201-H in intermediate B. It is important to note that H3 abstraction causes negative charge localization at O2 in intermediate B. The assistance

of proton wire KCX201-H_2O-H_2O-O2 (in transition state $B^{\neq}$) allows proton transfer to O2 to give the RuBP enolate shown in intermediate C.

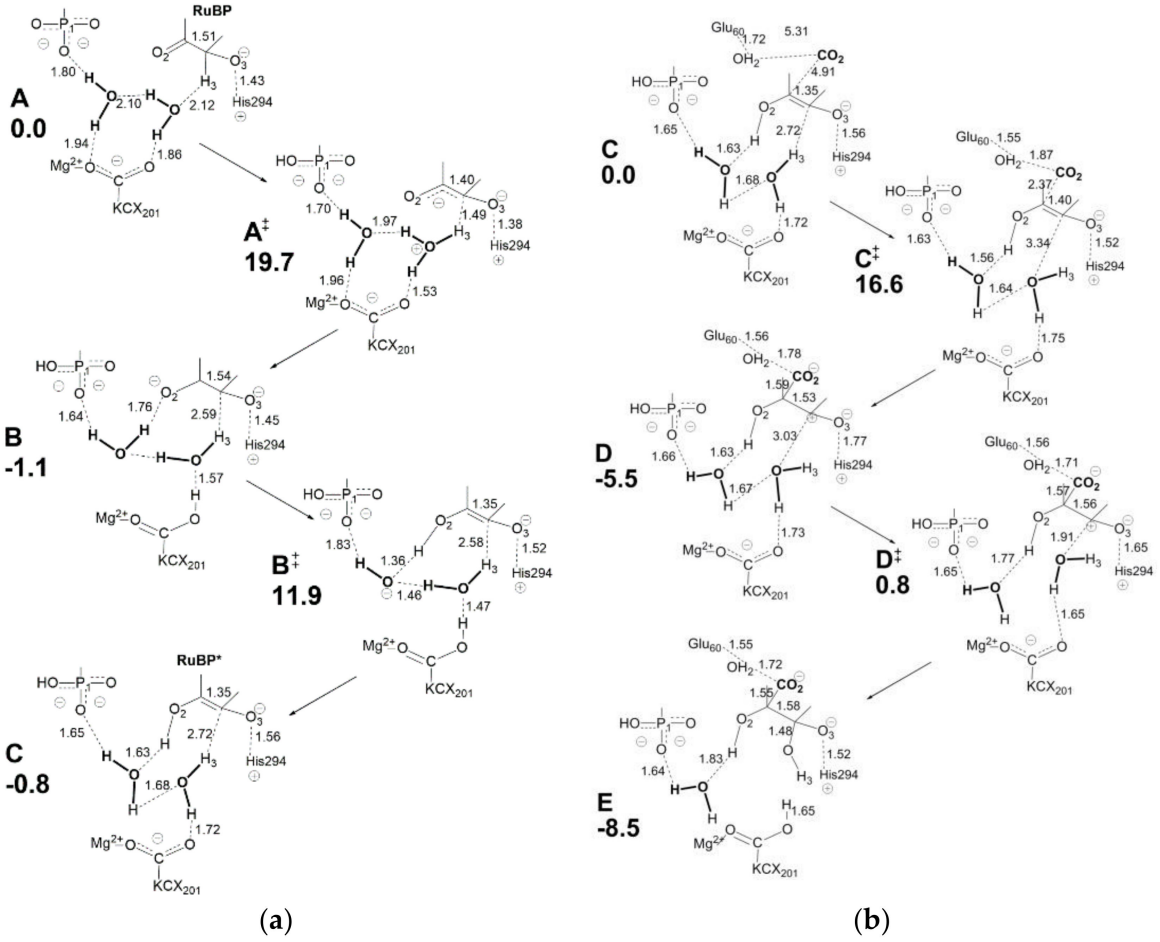

Figure 14. (**a**) Relative potential energies (in kcal/mol) of intermediates (B, C) and transition states ($A^{\neq}$, $B^{\neq}$) for RuBP enolization; (**b**) Relative potential energies of intermediates (C, D, E) and transition states ($C^{\neq}$, $D^{\neq}$) for the RuBP carboxylation and hydration steps. (Figure 14 from ref. [43], adapted and used by permission of American Chemical Society (copyright © 2020).

Considering Figure 14b, intermediate C shows a C2=C3 distance of 1.35 Å in agreement with formation of a double bond. The electron density associated with the C2=C3 bond is largely employed in a nucleophilic attack onto CO_2 affording intermediate **D** where C2-C3 distance (1.53 Å) and C2-CO2 distance (1.59 Å) agree with single bond formation. At the same time, a positive charge located at C3 triggers hydration by the vicinal water molecule (transition state $D^{\neq}$) while KCX201 accepts the excess proton producing the C3-gemdiolate in intermediate E. The model considers Glu60 (located at the loop 6) as being in protonated form and playing a role in stabilizing the 2-carboxy moiety through interaction with an additional water molecule.

Figure 15 displays the potential energy profile along the reaction coordinate calculated by using the B3LYP/6-31G* and B3LYP-gCP-D3 functional (represented in blue and orange color, respectively), compared with the experimental estimations of free-energy barriers (represented in black).

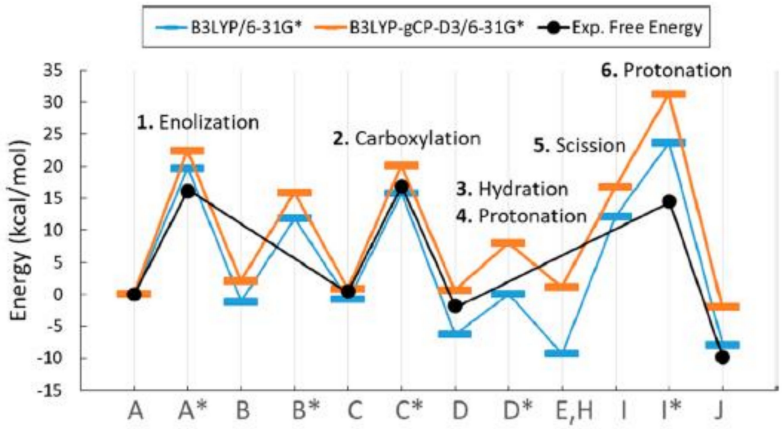

Figure 15. Blue and orange traits depict the potential energy (kcal/mol) profiles along the Rubisco carboxylase reaction as calculated by the B3LYP/6-31G* and the corresponding corrected B3LYP-gCP-D3 functional. Relevant reaction steps along the reaction coordinate are: (1.) RuBP enolization; (2.) carboxylation of the 2,3-enol(ate) intermediate; (3.) hydration of the 2-carboxy-3-keto-arabinitol-1,5-bisphosphate intermediate followed by protonation (4.); (5.) C2-C3 bond cleavage and (6.) protonation of C2. Black traits depict the potential energy (kcal/mol) profile indicated by experimental estimations of free-energy barriers. Figure 15 from ref. [43], used by permission of American Chemical Society (copyright © 2020)).

As shown in Figure 15, the experimental activation free energy (related to $k_{cat,C}$) is estimated at 16 kcal/mol [44,45] while calculated potential energy barriers are consistently higher, probably due to the error range for the approximate DFT methods.

Although not all the aspects of the proposed reaction mechanism find good interpretation, the model seems to provide a unique explanation for the a set of experimental evidence.

Mulholland et al. [46] tried to obtain more accurate estimation for the reaction electronic energy involved in the Rubisco carboxylation reaction by using the projector-based embedding technique (SCS-MP2/aug-cc-pVDZ method) applied to the model fragments constructed by the Gready group in 2008 (each model fragment composed of 77 atoms and 316 electrons). Although the selected computational method usually provides estimation of the activation and reaction energy close to that of the CCSD(T) method [47] when applied to enzyme active sites, the energy profile produced for the complete reaction coordinate (including carboxylation, hydration, dissociation and protonation reaction steps) seems not to agree with experimental results.

9. Rubisco Kinetics

From a bioenergetic point of view, the RuBP conversion into two 3PGA molecules catalyzed by Rubisco is spontaneous as the Gibbs free energy change (ΔG° as calculated by Faber et al. [48] at about -30 kcal mol^{-1}) allows the reaction to proceed without energy supply in the form of ATP, NAD(P)H or other reducing agents. Concerning the enzyme kinetics, experimental estimation of the activation free-energy barrier for the rate-limiting transition state is, as cited above, around 16 kcal/mol (at 298 K, for Rubisco from spinach). The corresponding maximal catalytic rate observed in vitro ($K_{cat,C}$) is 3–4 s^{-1}. However, the potential energy profile of the overall reaction appears quite complex (see Figure 15), therefore, over the last two decades, considerable effort has been made towards a complete description of the elementary steps and associated microscopic rate constants to assist in understanding enzyme kinetics.

Very recently Cummins and Gready [49] have described a detailed multistep mechanism for the Rubisco carboxylation and oxygenation reactions including microscopic rate constants associated with each elementary step (see Section S6, Figure S5). On the basis of the proposed mechanism the authors were able to derive equations that relate all measurable kinetic parameters such as $S_{C/O}$, $k_{cat,C}$, K_C, $k_{cat,O}$, and K_O (defined in Table S3)

to the microscopic rate constants. Moreover, the authors have calculated the expected values of dissociation rate constants for CO_2 and O_2 bound to the RuBP-enzyme complex. The kinetic model described by Cummins and Gready has been used by Milo et al., to draw important information about the variability of the $S_{C/O}$ selectivity factor among a large series of Rubisco enzymes (see later).

Before describing recent advances achieved by the Gready and Milo Research Groups, it is worthwhile citing previous studies developed by Tcherkez [50] and Tlusty [30], which started evidencing specific correlations between measurable kinetic parameters with the aim of finding specific adaptations during Rubisco evolution.

In an interesting study, Tcherkezet al. [50] have analyzed the $k_{cat,C}$ value of diverse Rubisco enzymes (see Figure 16a), evidencing an inverse relationship between $S_{C/O}$ and $k_{cat,C}$. This observation could be rationalized by proposing the qualitative energy profile along the reaction coordinate shown in Figure 16b.

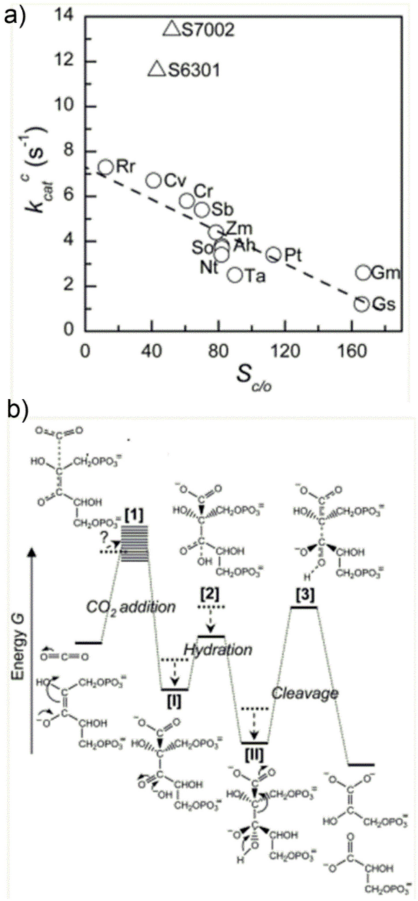

Figure 16. (**a**) $k_{cat,C}$ vs. $S_{C/O}$ dependence for various Rubiscos measured in vitro at 25 °C. The organisms from which the Rubiscos were isolated were: Ag, *Atriplex glabriuscula* (C3 dicot); Ah, *Amaranthus hybridus* (C4 dicot); Av, *Anabaena variabilis* (cyanobacterium); Cr, *Chlamydomonas reinhardtii* (green alga); Cv, *Chromatium vinosum* (bacterium); Eg, *Euglena gracilis* (green alga); Gm, *Griffithsia monilis* (red alga); Gs, *Galdieria sulfuraria* (red alga); Nt, *Nicotiana tabacum* (C3 dicot); Os, *Oryza sativa* (C3 monocot); Pt, *Phaeodactylum tricornutum* (diatom); Rr, *Rhodospirillum rubrum* (bacterium); Rs, the bacterial symbiont of the tubeworm *Riftia pachyptila*; Sb, *Sorghum bicolor* (C4 monocot); So, *Spinacia oleracea* (C3 dicot); S6301, *Synechococcus* PCC 6301 (cyanobacterium); S7002, *Synechococcus* PCC 7002 (cyanobacterium); Ta, *Triticum aestivum* (C3 monocot); and Zm, *Zea mays* (C4 monocot). Dotted line is a linear regression through all the data except for cyanobacteria (S6301 and S7002) which were excluded. (**b**) Energy profile along the Rubisco-catalyzed carboxylation reaction evidencing the structure of Transition States and Intermediates (Figure 16 from ref. [50], adapted and used by permission of PNAS (copyright © 2006)).

The major feature of the diagram shown in Figure 16b is the appearance of three energetic barriers (for the CO_2-addition reaction, carboxylic acid hydration and C2-C3-gemdiolate cleavage, respectively), with the "C2-C3-gemdiolate cleavage" barrier being the higher, which identifies the rate determining step. Most important, the authors have proposed that different Rubisco enzymes have evolved by optimizing the energetic profile in response to the CO_2:O_2 ratio available at the subcellular environment, which is characteristic of each species. Moreover, in order to increase the ability of Rubisco to discriminate between CO_2 and O_2 (enhancing thus the CO_2/O_2 specificity) the authors propose that the TS 1 for the CO_2-addition reaction (first energetic barrier in Figure 16b) must be product-like. In other words, the enzyme active site must possess a high affinity for the enediolate carboxylate TS 1 and, therefore, the ability to stabilize it in the energetic diagram. Under this hypothesis, the carboxy-ketone intermediate **[I]** and its gem-diol hydrate **[II]**, possessing a carboxylate-moiety, are proposed to bind tightly the active site undergoing energy stabilization. As a consequence, the energy stabilization of intermediate II causes an increase in the activation barrier for the subsequent C2-C3-gemdiolate cleavage-step, which is related to $k_{cat,C}$. On the whole, according to the author's hypothesis, an increase in CO_2/O_2 specificity is paid for with a slower rate of C2-C3 bond cleavage and, ultimately, with a slower overall reaction. The occurrence of these two coupled effects is cited in the literature as the "trade-off" between CO_2-specificity and reaction rate: the more the enzyme is specific for CO_2 (vs. O_2), the slower the overall carboxylation/hydration reaction and vice versa.

In 2010 Tlusty et al. [30] simplified the energetic profile proposed by Tcherkez et al., identifying two energetic "effective barriers" along the reaction coordinate corresponding to two irreversible steps which were identified as: (i) "effective gas binding" (encompassing RuBP enolization and subsequent CO_2/O_2 addition) described by the $k_{on,C}$ kinetic constants; (ii) "effective catalysis" (encompassing the C2-carboxylic acid hydrolysis and C2-C3 gemdiolate bond cleavage) described by $k_{cat,C}$ kinetic constant. Overall, Tlusty's study confirmed the negative power low correlation between specificity $S_{C/O}$ and $k_{cat,C}$.

The postulated "trade-off" between CO_2-specificity and carboxylation reaction rate of Rubisco was criticized by the capstone study published by Cummins and Gready in 2018 [49]. Giving a complete description of the reaction elementary steps and related microscopic kinetic constants, the study aimed at evaluating whether the Rubisco enzyme is tightly constrained by its active-site chemistry or whether the implementation of powerful tools as directed evolution techniques may have the opportunity to break the above cited "trade-off" and improve simultaneously both $k_{cat,C}$ and $S_{C/O}$ parameters. Results of the analysis point out that simultaneous improvement of CO_2-specificity and turnover rate is possible considered that, more likely, the stronger molecular constraint relay on the "activity-molecular stability" trade off. Moreover, the authors gave a complete derivation of the Michaelis-Menthen type rate, law for the Rubisco catalytic activity.

Very recently, the increased availability of measured kinetic parameters for the RuBP carboxylation and oxygenation reactions from a variety of C3- and C4-plants, algae (both green and red algae), bacteria and cyanobacteria allowed the analysis of a greater collection of data among different species.

Milo et al., have investigated the possible relationship between kinetic parameters measured for approximately 325 species at 25 °C and pH = 8 [51]. The analysis was developed by using the Rubisco reaction mechanism and nomenclature described by Cummins and Gready in 2018 [49] (see Section S6).

The qualitative energetic diagram shown in Figure 17a evidences that the carboxylation (line green profile) and oxygenation (line red profile) reactions proceed through two "effective" energetic barriers. Considering the carboxylation reaction after RuBP enolization, the first energetic barrier is related to CO_2-addition to the enediolate, while the second "rate limiting" energetic barrier is related to the C2-carboxylic acid hydration and C2-C3-gemdiolate bond cleavage (Figure 17a). Given standard assumptions, the authors

derived the catalytic efficiency (defined as k_{cat}/K_M) is related to the height of the first effective barrier, while k_{cat} is related to the second (Figure 17b).

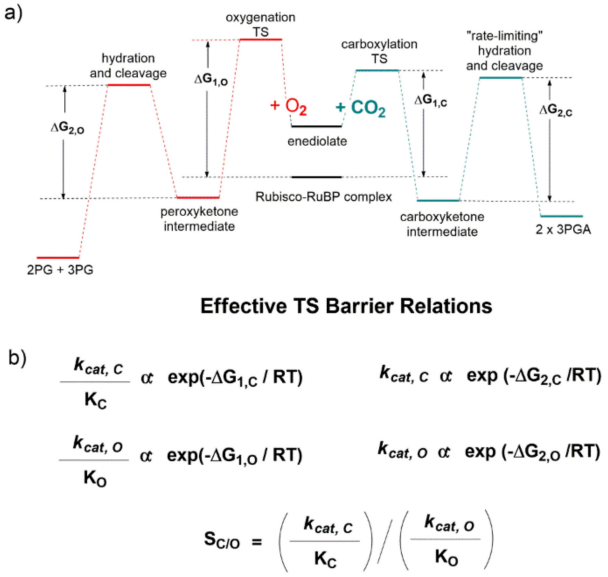

Figure 17. (**a**) The reaction coordinate diagram describes carboxylation (traits in green) and oxygenation (traits in red) reactions proceeding through two "effective" barriers. After Rubisco binding to the active site, the substrate undergoes enolization. The first effective barrier refers to the gas addition (CO_2 or O_2) to the enediolate, while, considering the carboxylation reaction, the second effective barrier (rate-limiting) encompasses C2-carboxylic acid hydration and C2-C3-gemdiolate bond cleavage reactions; (**b**) Given standard assumptions, the authors have concluded that catalytic efficiencies (k_{cat}/K_M) for the carboxylation and oxygenation reactions are related to the height of the first effective barrier while k_{cat} is related to the second effective barrier. (Figure 17 from ref. [51], adapted and used by permission of American Chemical Society (copyright © 2019)).

Thanks to the increased amount of kinetic data analyzed, Milo observed that the previously assessed strong $k_{cat,C}$-$S_{C/O}$ negative correlation was significantly weakened. The previously proposed correlation between $k_{cat,C}$ and K_C or $k_{cat,C}$ and $S_{C/O}$ appeared inconsistent if analyzed among a larger amount of data. An important outcome of the study was that a short range of variations clearly emerged for most kinetic parameters if analysed among organisms with similar physiology. For example, $k_{cat,C}$ showed variation by only 50% among Form I Rubiscos and $S_{C/O}$ showed variation of less than 30% among Form I Rubiscos (Figure 18a).

Considering the $S_{C/O}$ definition (see Table S3) the following power–law relationship could be derived: $\log(k_{cat,C}/K_C) = \log(k_{cat,O}/K_O) + \log(S_{C/O})$. When considering a set of data grouped for similar cellular physiology such as C3- and C4-plants and cyanobacteria (Figure 18b), having $S_{C/O}$ values roughly constant, experimentally a strong positive correlation was found between $k_{cat,C}/K_C$ and $k_{cat,O}/K_O$ (in a log–log diagram). As matter of fact, Form I Rubiscos display a high-confidence power-law relationship between $k_{cat,C}/K_C$ and $k_{cat,O}/K_O$ ($R = 0.94$, $p < 10^{-10}$).

Moreover, considering that the catalytic efficiencies for the carboxylation and oxygenation reactions are proportional to $\Delta G_{1,C}$ and $\Delta G_{1,O}$, respectively, ($\Delta G_{1,C}$ and $\Delta G_{1,O}$ are shown in Figure 17a), the following relationship must hold: $\Delta G_{1,C} = \Delta G_{1,O} + C$. As a consequence of this relationship, at the active site molecular level every factor causing a decrease of the CO_2-addition barrier ($\Delta G_{1,C}$) causes, at the same time, an approximately equal decrease in the O_2-addition barrier ($\Delta G_{1,O}$).

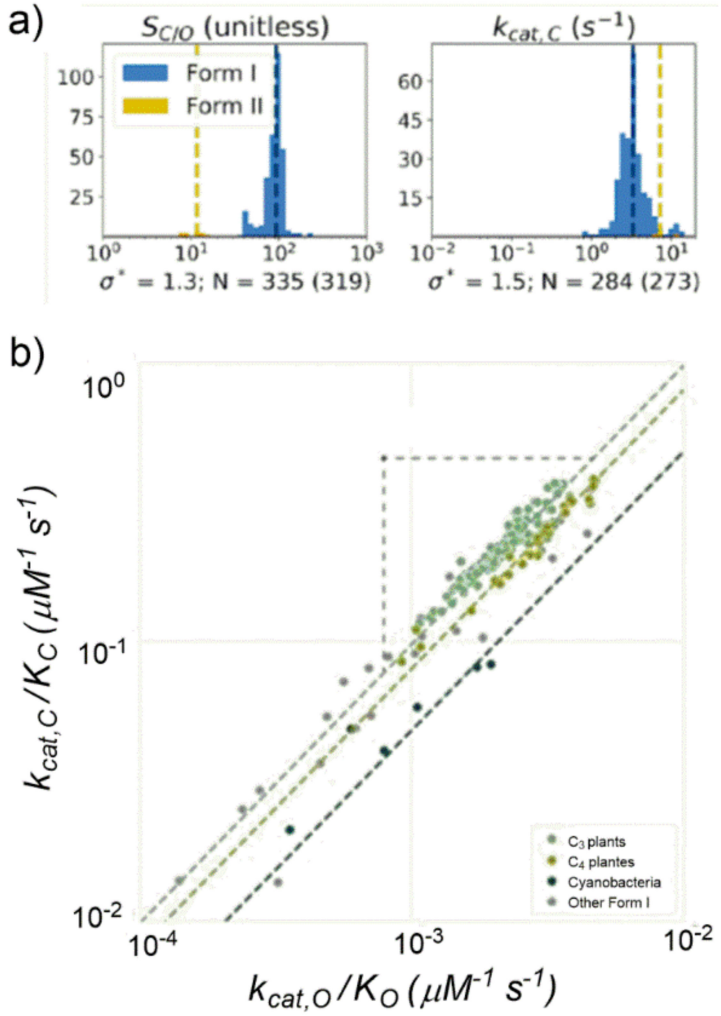

Figure 18. (**a**) Histograms of Rubisco kinetic parameters $S_{C/O}$ and $k_{cat,C}$ experimentally determined for several hundred species at 25 °C and pH = 8. The values of kinetic parameters are reported along the *X*-axis (log scale) and the number of data points is reported along the *Y*-axis. The parameter distributions for Form I Rubisco are represented in blue while the parameter distributions for Form II Rubisco are represented in yellow. Dashed lines give the median value. N is the number of Form I Rubisco for which $S_{C/O}$ and $k_{cat,C}$ parameters have been considered and σ* is the multiplicative standard deviation of Form I values; (**b**) diagram showing $k_{cat,C}/K_C$ and $k_{cat,O}/K_O$ are strongly correlated on a log−log scale (R = 0.94; $p < 10^{-10}$). Light green point refers to Rubisco from C3 plants; mustard points refer to Rubisco from C4 plants; deep green points refer to Rubisco from cyanobacteria. (Figure 18 from ref. [51], adapted and used by permission of American Chemical Society (copyright © 2019)).

10. Photorespiration

As described above, according to the recent study published by Milo et al., the catalytic efficiencies of the carboxylation and oxygenation reactions are strictly related. Photosynthetic organisms (such as plants and bacteria) with similar cellular physiology have adapted to share similar $S_{C/O}$ selectivity. This observation can indirectly indicate that efforts aiming at improving $S_{C/O}$ value by directed mutagenesis would probably be unproductive.

However, a recent study from the Farquhar Group [12] opened a new research scenario, having evidenced the existence of biochemical links between the photosynthesis and photorespiration pathways. The study shed a new light on the photorespiration process and some of its beneficial features, giving a possible explanation as to why photosynthetic

organisms have evolved by "tolerating" the oxygenation reaction instead of "eliminating" this side reaction.

Over the last four decades, according to the Farquhar et al., (FvCB model) photosynthesis model, [11] the RuBP-oxygenation reaction leading to 2-phosphoglycolate production has been considered a deleterious process, as the toxic intermediate 2-phosphoglycolate must be rapidly metabolized by the photorespiratory metabolism causing the following two drawbacks: (i) reduction of RuBP available for the carboxylation reaction; (ii) recycle of glycolate back to RuBP in a process that co-produces CO_2 and NH_3. CO_2 is usually released from leaf while NH_3 recycling is energetically costly. Overall, approximately 2 mol of 2-phosphoglycolate produced undo one carboxylation reaction, causing a decrease of carbon fixation efficiency into hexose sugars by up to 50%. However, the recent study points out that photorespiratory metabolism increases de novo nitrogen uptake (as NO_3^-) and reduction (to NH_4^+) by terrestrial plants, increasing availability of the precious element that enters the 2-oxo-glutarate/glutamic acid cycle harnessing, thus, glyoxylate conversion into glycine (Figure 19). Therefore, the negative effect due to reduced CO_2-fixation into hexose sugars is counterbalanced by an increased synthesis of glycine that is partially converted into serine. Overall, photorespiration, despite reducing the Rubisco carboxylation efficiency, seems to improve the overall photosynthetic performance.

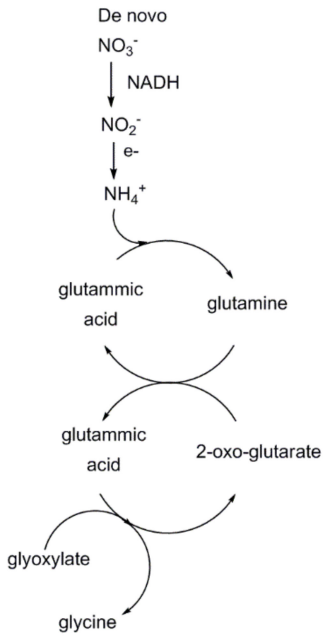

Figure 19. The newly proposed metabolic link between photorespiration and photosynthesis. The novo absorbed NO_3^- is reduced by NADH and electron transport to NH_4^+ in leaves. In chloroplasts NH_4^+converts glutamic acid into glutamine that converts 2-oxo-glutarate to glutammic acid. Then glutamic acid is transported in peroxisomes where reaction with glyoxylate produces 2-oxo-glutarate and glycine. Considering that glyoxylate derives from 2-phosphoglycolate (2PG) which is dephosphorylated to glycolate and oxidized to glyoxylate in peroxisomes, overall, the novo absorbed NO_3^- and glyoxylate are ultimately converted into glycine. (Previously unpublished figure).

11. Conclusions

As mentioned in the introductory section, the steady increase over the last century of the CO_2-fertilization effect due to increase of atmospheric CO_2 concentration (G_{ATM}) is considered the largest contributor (among others) to the modelled GPP increase by terrestrial plants and, ultimately, to the terrestrial CO_2-sink (S_{LAND}) ability.

In a recent study Farquhar et al. [4] on the basis of various Terrestrial Biosphere Models (TBM), have shown that GPP (expressed in units of Gt of carbon atoms fixed annually by plants at global level) has constantly increased from approximately 105 $GtCy^{-1}$ estimated

in 1900 to approximately 140 $GtCy^{-1}$ estimated in 2010. According to these models, approximately 135 $GtCy^{-1}$ fixed into plant biomass in 2010 are due to the CO_2-fertilization effect that accounts for a 30% increase with respect to the value estimated in 1900.

Moreover, Farquhar identifies two main components as contributing to the CO_2-fertilization effect: (i) the CO_2 greening effect; (ii) the CO_2 leaf-level effect. The CO_2 greening effect is defined as "the increased light harvesting capacity due to the investment of additional plant carbon in a higher leaf area" while the CO_2 leaf-level effect is "the CO_2-induced increase in GPP that occurs at constant leaf area". The leaf level effect, in turn, includes the direct biochemical effect of increased atmospheric CO_2 on the Rubisco carboxylase activity.

According to the Farquhar's study and other related research [52,53], terrestrial plants have shown a significant natural ability to adapt to increased CO_2-concentration over the last century. The development of more advanced TBMs taking into account the plant coordination of photosynthesis [54] will probably give a better estimation of plant's potential for CO_2-removal in the near future.

Supplementary Materials: The following are available online at https://www.mdpi.com/article/10.3390/catal11070813/s1, Table S1: Cumulative CO_2 for different time of periods in GtC; Table S2: Decadal mean in the five components of the anthropogenic CO_2 budget for different periods and the last year; Table S3: Definition of Rubisco kinetic parameters; Scheme S1: A schematic representation of the Calvin-Benson-Bassham (CBB) cycle active in photosynthetic organisms; Scheme S2: Connectivity diagram showing the secondary structure of the large subunit of Rubisco; Figure S1: Combined components of the global carbon budget illustrated as a function of time; Figure S2: Small subunit sequences aligned according to Rubisco x-ray crystal structures; Figure S3: Ribbon representation of the secondary structure elements of S subunit of *Chlamydomonas* Rubisco; Figure S4: Cumulative CO_2 and O_2 density around the active site of Rubisco; Figure S5: The mechanism of RuBP enolization, with description of the RuBP complete oxygenation and complete carboxylation reactions following the nomenclature of Cummins et al. [49].

Funding: The University of Bari Aldo Moro is acknowledged for its financial support (Fondi di Ateneo, 2018).

Conflicts of Interest: The authors declare no conflict of interest.

References and Note

1. Masson-Delmotte, V.; Zhai, P.; Portner, H.-O.; Roberts, D.; Skea, J.; Shukla, P.R.; Pirani, A.; Moufouma-Okia, W.; Pean, C.; Pidcock, R.; et al. Global Warming of 1.5 °C. An IPCC Special Report on the Impacts of Global Warming of 1.5 °C above Pre-Industrial Levels and Related Global Greenhouse Gas Emission Pathways, in the Context of Strengthening the Global Response to the Threat of Climate Change, Sustainable Development, and Efforts to Eradicate Poverty. 2018. Available online: https://www.ipcc.ch/sr15/ (accessed on 30 June 2021).
2. Friedlingstein, P.; O'Sullivan, M.; Jones, M.W.; Andrew, R.M.; Hauck, J.; Olsen, A.; Peters, G.P.; Peters, W.; Pongratz, J.; Sitch, S.; et al. Global Carbon Budget 2020. *Earth Syst. Sci. Data* **2020**, *12*, 3269–3340. [CrossRef]
3. Liu, Y.; Piao, S.; Gasser, T.; Ciais, P.; Yang, H.; Wang, H.; Keenan, T.F.; Huang, M.; Wan, S.; Song, J.; et al. Field-experiment constraints on the enhancement of the terrestrial carbon sink by CO_2 fertilization. *Nat. Geosci.* **2019**. [CrossRef]
4. Haverd, V.; Smith, B.; Canadell, J.G.; Cuntz, M.; Mikaloff-Fletcher, S.; Farquhar, G.; Woodgate, W.; Briggs, P.R.; Trudinger, C.M. Higher than expected CO_2 fertilization inferred from leaf to global observations. *Glob. Change Biol.* **2020**, *26*, 2390–2402. [CrossRef]
5. O'Sullivan, M.; Spracklen, D.V.; Batterman, S.A.; Arnold, S.R.; Gloor, M.; Buermann, W. Have Synergies Between Nitrogen Deposition and Atmospheric CO_2 Driven the Recent Enhancement of the Terrestrial Carbon Sink? *Glob. Biogeochem. Cycles* **2019**, *33*, 163–180.
6. Bar-On, Y.M.; Milo, R. The global mass and average rate of Rubisco. *Proc. Natl. Acad. Sci. USA* **2019**, *116*, 4738–4743. [CrossRef]
7. Von Caemmerer, S. Rubisco carboxylase/oxygenase: From the enzyme to the globe: A gas exchange perspective. *J. Plant Physiol.* **2020**, *252*, 153240. [CrossRef]
8. Rogers, A.; Medlyn, B.E.; SDukes, J.; Bonan, G.; von Caemmerer, S.; Dietze, M.C.; Kattge, J.; Leakey, A.D.B.; Mercado, L.M.; Niinemets, Ü.; et al. A roadmap for improving the representation of photosynthesis in Earth system models. *New Phytol.* **2017**, *213*, 22–42. [CrossRef]
9. López-Calcagno, P.E.; Brown, K.L.; Simkin, A.J.; Fisk, S.J.; Vialet-Chabrand, S.; Lawson, T.; Raines, C.A. Stimulating photosynthetic processes increases productivity and water-use efficiency in the field. *Nat. Plants* **2020**, *6*, 1054–1063. [CrossRef]

10. Berg, I.A.; Kockelkorn, D.; Ramos-Vera, W.H.; Say, R.; Zarzycki, J. *Carbon Dioxide as Chemical Feedstock*; Aresta, M., Ed.; Wiley-VCH Verlag GmbH & Co. KGaA: Weinheim, Germany, 2010; Chapter 3; pp. 33–53.
11. Farquhar, G.D.; von Caemmerer, S.; Berry, J.A. A Biochemical Model of Photosynthetic CO_2 Assimilation in Leaves of C3 Species. *Planta* **1980**, *149*, 78–90. [CrossRef]
12. Busch, F.A.; Sage, R.F.; Farquhar, G.D. Plants increase CO_2 uptake by assimilating nitrogen via the photorespiratory pathway. *Nat. Plants* **2018**, *4*, 46–54. [CrossRef]
13. Andersson, I.; Backlund, A. Structure and function of Rubisco. *Plant Physiol. Biochem.* **2008**, *46*, 275–291. [CrossRef] [PubMed]
14. Loewen, P.C.; Didychuk, A.L.; Switala, J.; Perez-Luque, R.; Fitac, I.; Loewen, M.C. Structure of *Pisumsativum* Rubisco with bound ribulose 1,5-bisphosphate. *Acta Crystallogr. Sect. F Struct. Biol. Cryst. Commun.* **2013**, *F69*, 10–14. [CrossRef]
15. Stec, B. Structural mechanism of RuBisCO activation by carbamylation of the active site lysine. *Proc. Natl. Acad. Sci. USA* **2012**, *109*, 18785–18790. [CrossRef] [PubMed]
16. Satagopan, S.; Chan, S.; Perry, L.J.; Tabita, F.R. Structure-Function Studies with the Unique Hexameric Form II Ribulose-1,5-bisphosphate Carboxylase/Oxygenase (Rubisco) from *Rhodopseudomonas palustris*. *J. Biol. Chem.* **2014**, *289*, 21433–21450. [CrossRef]
17. Valegard, K.; Hasse, D.; Andersson, I.; Gunn, L.H. Structure of Rubisco from Arabidopsis thaliana in complex with 2-carboxyarabinitol-1,5-bisphosphate. *Acta Crystallogr. Sect. F Struct. Biol. Cryst. Commun.* **2018**, *D74*, 1–9.
18. Chapman, M.S.; Suh, S.W.; Cascio, D.; Smith, W.W.; Eisenberg, D. Sliding-layer conformational change limited by the quaternary structure of plant RuBisCO. *Nature* **1987**, *329*, 354–356. [CrossRef] [PubMed]
19. Andersson, I.; Taylor, T.C. Structural framework for catalysis and regulation in ribulose-1,5-bisphosphate carboxylase/oxygenase. *Arch. Biochem. Biophys.* **2003**, *414*, 130–140. [CrossRef]
20. Kellogg, E.A.; Juliano, N.D. The structure and function of Rubisco and their implication for systematic studies. *Am. J. Bot.* **1997**, *84*, 413–428. [CrossRef]
21. Tang, Y.-C.; Chang, H.-C.; Roeben, A.; Wischnewski, D.; Wischnewski, N.; Kerner, M.J.; Hartl, F.U.; Hayer-Hartl, M. Structural Features of the GroEL-GroES Nano-Cage Required for Rapid Folding of Encapsulated Protein. *Cell* **2006**, *125*, 903–914. [CrossRef]
22. Genkov, T.; Spreitzer, R.J. Highly Conserved Small Subunit Residues Influence Rubisco Large Subunit Catalysis. *J. Biol. Chem.* **2009**, *284*, 30105–30112. [CrossRef]
23. Spreitzer, R.J. Role of the small subunit in ribulose-1,5-bisphosphate carboxylase/oxygenase. *Arch. Biochem. Biophys.* **2003**, *414*, 141–149. [CrossRef]
24. Joshi, J.; Mueller-Cajar, O.; Tsai, Y.-C.C.; Hartl, F.U.; Hayer-Hartl, M. Role of Small Subunit in Mediating Assembly of Red-type Form I Rubisco. *J. Biol. Chem.* **2015**, *290*, 1066–1074. [CrossRef]
25. Fukayama, H.; Kobara, T.; Shiomia, K.; Morita, R.; Sasayama, D.; Hatanaka, T.; Azuma, T. Rubisco small subunits of C4 plants, Napier grass and guinea grass confer C4-like catalytic properties on Rubisco in rice. *Plant Prod. Sci.* **2019**, *22*, 296–300. [CrossRef]
26. Matsumura, H.; Shiomi, K.; Yamamoto, A.; Taketani, Y.; Kobayashi, N.; Yoshizawa, T.; Tanaka, S.; Yoshikawa, H.; Endo, M.; Fukayama, H. Hybrid Rubisco with Complete Replacement of Rice Rubisco Small Subunits by Sorghum Counterparts Confers C4 Plant-like High Catalytic Activity. *Mol. Plant* **2020**, *13*, 1570–1581. [CrossRef]
27. Lin, M.T.; Stone, W.D.; Chaudhari, V.; Hanson, M.R. Small subunits can determine enzyme kinetics of tobacco Rubisco expressed in *Escherichia coli*. *Nat. Plants* **2020**, *6*, 1289–1299. [CrossRef]
28. Martin-Avilaa, E.; Lima, Y.-L.; Bircha, R.; Dirkb, L.M.A.; Bucka, S.; Rhodesa, T.; Sharwooda, R.; Kapralovc, M.V.; Whitneya, S.M. Modifying Plant Photosynthesis and Growth via Simultaneous Chloroplast Transformation of Rubisco Large and Small Subunits. *Plant Cell* **2020**, *32*, 2898–2916. [CrossRef]
29. Wilson, R.H.; Whitney, S.M. Improving CO_2 Fixation by Enhancing Rubisco Performance. In *Directed Enzyme Evolution: Advances and Applications*; Alcalde, M., Ed.; Springer International Publishing AG: Berlin/Heidelberg, Germany; Cham, Switzerland, 2017; Chapter 4.
30. Savir, Y.; Noor, E.; Milo, R.; Tlusty, T. Cross-species analysis traces adaptation of Rubisco toward optimality in a low-dimensional landscape. *Proc. Natl. Acad. Sci. USA* **2010**, *107*, 3475–3480. [CrossRef] [PubMed]
31. Van Lun, M.; Hub, J.S.; van der Spoel, D.; Andersson, I. CO_2 and O_2 Distribution in Rubisco Suggests the Small Subunit Functions as a CO_2 Reservoir. *J. Am. Chem. Soc.* **2014**, *136*, 3165–3171. [CrossRef] [PubMed]
32. Poudel, S.; Pike, D.H.; Raanan, H.; Mancini, J.A.; Nandab, V.; Rickaby, R.E.M.; Falkowski, P.G. Biophysical analysis of the structural evolution of substrate specificity in RuBisCO. *Proc. Natl. Acad. Sci. USA* **2020**. [CrossRef]
33. Taylor, T.C.; Andersson, I. The structure of the complex between rubisco and its natural substrate ribulose-1,5-bisphosphate. *J. Mol. Biol.* **1997**, *265*, 432–444. [CrossRef]
34. Lundqvist, T.; Schneider, G. Crystal-structure of activated ribulose-1,5- bisphosphate carboxylase complexed with its substrate, ribulose-1,5- bisphosphate. *J. Biol. Chem.* **1991**, *266*, 12604–12611. [CrossRef]
35. Andersson, I. Large structures at high resolution: Spinach ribulose-1,5- bisphosphate carboxylase/oxygenase at 1.6 Å resolution. *J. Mol. Biol.* **1996**, *259*, 160–174. [CrossRef]
36. Knight, S.; Knight, S.; Andersson, I.; Branden, C.-I. Crystallographic Analysis of Ribulose 1,5-Bisphosphate Carboxylase from Spinach at 2.4 Å Resolution. Subunit Interactions and Active Site. *J. Mol. Biol.* **1990**, *215*, 113–160. [CrossRef]
37. Kannappan, B.; Gready, J.E. Redefinition of Rubisco carboxylase reaction reveals origin of water for hydration and new roles for active-site residues. *J. Am. Chem. Soc.* **2008**, *130*, 15063–15080. [CrossRef]

38. Duff, A.P.; Andrews, T.J.; Curmi, P.M.G. The Transition between the Open and Closed States of Rubisco is Triggered by the Inter-Phosphate Distance of the Bound Bisphosphate. *J. Mol. Biol.* **2000**, *298*, 903–916. [CrossRef] [PubMed]
39. Marcus, Y.; Altman-Gueta, H.; Finkler, A.; Gurevitz, M. Mutagenesis at Two Distinct Phosphate-Binding Sites Unravels Their Differential Roles in Regulation of Rubisco Activation and Catalysis. *J. Bacteriol.* **2005**, *187*, 4222–4228. [CrossRef] [PubMed]
40. Cleland, W.W.; Andrews, T.J.; Gutteridge, S.; Hartman, F.G.; Lorimer, G.H. Mechanism of Rubisco: The Carbamate as General Base. *Chem. Rev.* **1998**, *98*, 549–561. [CrossRef] [PubMed]
41. Cummins, P.L.; Kannappan, B.; Gready, J.E. Revised Mechanism of Carboxylation of Ribulose-1,5-Biphosphate by Rubisco from Large Scale Quantum Chemical Calculations. *J. Comput. Chem.* **2018**, *39*, 1656–1665. [CrossRef]
42. Cummins, P.L.; Kannappan, B.; Gready, J.E. Ab Initio Molecular Dynamics Simulation and Energetics of the Ribulose-1,5-biphosphate Carboxylation Reaction Catalysed by Rubisco: Towards Elucidating the Stereospecific Protonation Mechanism. *J. Phys. Chem. B* **2019**, *123*, 2679–2686. [CrossRef]
43. Cummins, P.L.; Gready, J.E. Kohn–Sham Density Functional Calculations Reveal Proton Wires in the Enolization and Carboxylase Reactions Catalyzed by Rubisco. *J. Phys. Chem. B* **2020**, *124*, 3015–3026. [CrossRef]
44. McNevin, D.; von Caemmerer, S.; Farquhar, G. Determining RuBisCO activation kinetics and other rate and equilibrium constants by simultaneous multiple non-linear regression of a kinetic model. *J. Exp. Bot.* **2006**, *57*, 3883–3900. [CrossRef]
45. Tcherkez, G.G.B.; Bathellier, C.; Stuart-Williams, H.; Whitney, S.; Gout, E.; Bligny, R.; Badger, M.; Farquhar, G.D. D_2O Solvent Isotope Effects Suggest Uniform Energy Barriers in Ribulose-1,5-bisphosphate Carboxylase/Oxygenase Catalysis. *Biochemistry* **2013**, *52*, 869–877. [CrossRef]
46. Douglas-Gallardo, O.A.; Shepherd, I.; Bennie, S.J.; Ranaghan, K.E.; Mulholland, A.J.; Vöhringer-Martinez, E. Electronic structure benchmark calculations of CO_2 fixing elementary chemical steps in RuBisCO using the projector based embedding approach. *J. Comput. Chem.* **2020**, *41*, 2151–2157. [CrossRef]
47. Ranaghan, K.E.; Shchepanovska, D.; Bennie, S.J.; Lawan, N.; Macrae, S.J.; Zurek, J.; Manby, F.R.; Mulholland, A.J. Projector-Based Embedding Eliminates Density Functional Dependence for QM/MM Calculations of Reactions in Enzymes and Solution. *J. Chem. Inf. Model.* **2019**, *59*, 2063–2078. [CrossRef] [PubMed]
48. Glueck, S.M.; Gümüs, S.; Fabian, W.M.F.; Faber, K. Biocatalytic carboxylation. *Chem. Soc. Rev.* **2010**, *39*, 313–328. [CrossRef]
49. Cummins, P.L.; Kannappan, B.; Gready, J.E. Directions for Optimization of Photosynthetic Carbon Fixation: RuBisCO's Efficiency May Not Be So Constrained After All. *Front. Plant Sci.* **2018**, *9*, 183. [CrossRef]
50. Tcherkez, G.G.B.; Farquhar, G.D.; Andrews, T.J. Despite slow catalysis and confused substrate specificity, all ribulose bisphosphate carboxylases may be nearly perfectly optimized. *Proc. Natl. Acad. Sci. USA* **2006**, *103*, 7246–7251. [CrossRef] [PubMed]
51. Flamholz, A.I.; Prywes, N.; Moran, U.; Davidi, D.; Bar-On, Y.M.; Oltrogge, L.M.; Alves, R.; Savage, D.; Milo, R. Revisiting Trade-offs between Rubisco Kinetic Parameters. *Biochemistry* **2019**, *58*, 3365–3376. [CrossRef] [PubMed]
52. Campbell, J.E.; Berry, J.A.; Seibt, U.; Smith, S.J.; Montzka, S.A.; Launois, T.; Belviso, S.; Bopp, L.; Laine, M. Large historical growth in global terrestrial gross primary production. *Nature* **2017**, *544*, 84–87. [CrossRef] [PubMed]
53. Wang, H.; Prentice, I.C.; Keenan, T.F.; Davis, T.W.; Wright, I.J.; Cornwell, W.K.; Evans, B.J.; Peng, C. Towards a universal model for carbon dioxide uptake by plants. *Nat. Plants* **2017**. [CrossRef] [PubMed]
54. Note: According to the definition by Farquhar (see reference [4]) the "coordination photosynthesis theory" consider that plants optimize their productivity in their environment through relative nitrogen investment in electron transport and Rubisco limited steps such that they are co-limiting.